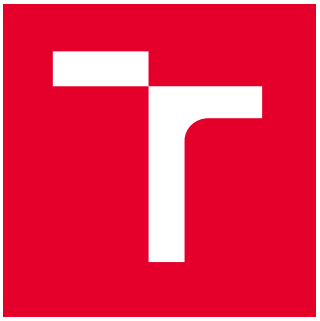

BRNO UNIVERSITY OF TECHNOLOGY

VYSOKÉ UČENÍ TECHNICKÉ V BRNĚ

FACULTY OF MECHANICAL ENGINEERING

FAKULTA STROJNÍHO INŽENÝRSTVÍ

INSTITUTE OF PHYSICAL ENGINEERING

ÚSTAV FYZIKÁLNÍHO INŽENÝRSTVÍ

COMPARISON OF ABSORPTIVE MODEL OF ELECTRON SCATTERING TO FROZEN PHONON MODEL CALCULATIONS

POROVNÁNÍ ABSORPČNÍHO MODELU ROZPTYLU ELEKTRONŮ S MODELEM ZAMRZLÝCH FONONŮ

MASTER'S THESIS

DIPLOMOVÁ PRÁCE

AUTHOR — **Bc. Martin Hájek**

AUTOR PRÁCE

SUPERVISOR — **doc. RNDr. Ján Rusz, Ph.D.**

VEDOUCÍ PRÁCE

BRNO 2025

BRNO UNIVERSITY OF TECHNOLOGY
FACULTY OF MECHANICAL ENGINEERING

Assignment Master's Thesis

Institut:	Institute of Physical Engineering
Student:	**Bc. Martin Hájek**
Degree programm:	Physical Engineering and Nanotechnology
Branch:	no specialisation
Supervisor:	**doc. RNDr. Ján Rusz, Ph.D.**
Academic year:	2024/25

As provided for by the Act No. 111/98 Coll. on higher education institutions and the BUT Study and Examination Regulations, the director of the Institute hereby assigns the following topic of Master's Thesis:

Comparison of absorptive model of electron scattering to frozen phonon model calculations

Brief Description:

In transmission electron microscope imaging, the electrons undergo the effect of inelastic scattering primarily due to phonon excitations. To incorporate the effects of inelastic scattering on the elastic scattering, absorptive effects have to be included in the modeling of the electron propagation hence the gradual decrease in intensity of the elastic channel of the electron beam. Various methodologies regarding absorption effects exist. In this thesis, we compare the widely used complex absorptive potentials method to the more elaborate frozen phonon model coming from correlated atomic motion and the Einstein model of atomic motion, respectively.

Master's Thesis goals:

1) Summarize the current understanding of the process of elastic scattering in transmission electron microscopy, with a focus on the effects of atomic vibrations.
2) Computationally compare the elastic scattering channel calculated by the absorptive potential model with calculations explicitly containing the atomic vibrations, both within an Einstein model and a correlated model.
3) Explore the relevant parts of parameter space, such as the mass of elements, convergence and collection angles, and discuss the limits of validity of the absorptive potential model.

Recommended bibliography:

YOSHIOKA, Hide. Effect of Inelastic Waves on Electron Diffraction. Online. Journal of the Physical Society of Japan. 1957, 12, 6, 618-628. ISSN 0031-9015.

WEICKENMEIER, A. and KOHL, H. Computation of absorptive form factors for high-energy electron diffraction. Online. Acta Crystallographica Section A Foundations of Crystallography. 47, 5, 590-597. ISSN 01087673.

FINDLAY, S. D.; OXLEY, M. P. and ALLEN, L. J. Modeling Atomic-Resolution Scanning Transmission Electron Microscopy Images. Online. Microscopy and Microanalysis. 2008, 14, 1, 48-59. ISSN 1431-9276.

MARTIN, A. V.; FINDLAY, S. D. and ALLEN, L. J. Model of phonon excitation by fast electrons in a crystal with correlated atomic motion. Online. Physical Review B. 2009, 80, 2. ISSN 1098-0121.

LUGG, N. R.; FORBES, B. D.; FINDLAY, S. D. and ALLEN, L. J. Atomic resolution imaging using electron energy-loss phonon spectroscopy. Online. Physical Review B. 2015, 91, 14. ISSN 1098-0121.

Deadline for submission Master's Thesis is given by the Schedule of the Academic year 2024/25

In Brno,

L. S.

prof. RNDr. Tomáš Šikola, CSc. Director of the Institute	doc. Ing. Jiří Hlinka, Ph.D. FME dean

Abstract

In transmission electron microscope imaging, the electrons undergo the effects of inelastic scattering primarily due to phonon excitations. Effects of inelastic scattering cause a gradual decrease in the intensity of the elastic scattering component of the electron beam. We thus need a good model of absorption in order to accurately simulate TEM images. In the thesis we utilize the quantum scattering theory and compare two frozen phonon models and complex absorptive model of absorption via results from extensive multislice simulations and molecular dynamics simulations.

Keywords

electron scattering, absorption model, frozen phonon model, transmission electron microscopy

Abstrakt

Při zobrazování v transmisní elektronové mikroskopii dochází při interakci elektronů se vzorkem k neelastickému rozptylu vlivem excitací fononů. Efekty neelastického rozptylu pak zapříčiní snížení intenzity elastické složky elektronového svazku. Při simulaci TEM obrazu je proto důležité užívat správný absorpční model. V této práci využíváme kvantové teorie rozptylu a porovnáváme dva modely takzvaných zamrznutých fononů vůči komplexnímu absorptivnímu modelu za pomoci výsledků z rozsáhlých multislice simulací a molekulární dynamiky.

Klíčová slova

rozptyl elektronů, absorpční model, model zamrznutých fononů, transmisní elektronová mikroskopie

HÁJEK, Martin. *Comparison of absorptive model of electron scattering to frozen phonon model calculations.* Master's Thesis. Ján RUSZ (supervisor). Brno: Brno University of Technology, Faculty of Mechanical Engineering, 2025. Available at:
https://www.vut.cz/en/students/final-thesis/detail/166097.

Hereby I declare that I wrote the diploma thesis *Comparison of absorptive model of electron scattering to frozen phonon model calculations* by myself under the supervision of doc. RNDr. Ján Rusz, Ph.D., all sources and references are cited and listed in Bibliography section. This work was created with the help of generative AI model ChatGPT, which was used for text formatting. In case of using AI, the generated text has been reviewed and checked, and I take full responsibility for the text in the thesis.

Bc. Martin Hájek

Acknowledgements

One big Thanks belongs to my supervisor Ján Rusz, not only for the enjoyable talks, discussions, and successfully guiding me through the writing of this thesis, but also for the wonderful opportunity to work with You and Your amazing group at Uppsala University, where I have been warmly welcomed. Also, Thanks to all the friends at Uppsala, who always kindly helped me whenever I needed, and for the fun we had inside or outside of academia.

I also cannot forget to express my great Gratitude, which belong to Andrea Konečná, who introduced me to the topics of electron microscopy and led me from almost the beginning of my university studies. In my five-year studies at FyzING, I have always been accompanied by great friends, and together, with the help of our mutual support, we overcame all the obstacles we faced, and for this, I am very grateful to them.

Lastly I have to say Thanks to my parents, *mým rodičům Děkuji za tu nekončící, nevyčerpatelnou podporu, kterou mi dáváte* ♡.

The thesis was written with the support of the Czech Science Foundation GAČR under the Junior Star grant No. 23-05119M.

Contents

Introduction

Electron microscopy is a rapidly developing field and plays a significant role in many scientific applications such as material science, the semiconductor industry, or biosciences. Instrumentation development and aberration correction of the last couple of decades allowed us to acquire an image of the specimen with atomic resolution [1, 2]. With additional equipment, such as energy filters, we are capable of atomic resolution spectroscopies, for example, the electron energy loss spectroscopy [3, 4, 5].

The instrument that reaches the highest resolution in electron microscopy is the transmission electron microscope **(TEM)** and its modification, capable of operating in scanning mode, so-called scanning transmission electron microscope **(STEM)**. TEMs accelerate electrons to energies ranging from tens of keV up to MeV. At such energies, the electron wavelength is significantly shorter than the inter-atomic distances. Yet, it is difficult to obtain resolution beyond the capabilities mentioned in [1], which means that the effect of diffraction, due to the wave-like properties of electrons, is not the primary limitation of electron imaging. Instead, the resolution limitation in aberration-corrected systems comes from specimen-related factors such as thermal vibration effects, which may cause smearing of the image. [6]

A comprehensive understanding of image formation requires a detailed description of the system, i.e., electron optics, and the electron-specimen interaction, which govern the contrast and resolution in transmission electron microscopy imaging. The understanding enables us to predict the correct electron optics setup and the shape of the traversing electron wave function. The implementation of the theory of image formation and specimen-related effects helps us to direct the development of new instrumentation as well as research in material sciences. With powerful computers and software that utilize the theory, we can significantly speed up the process of research. [7, 8]

This thesis primarily focuses on the theoretical framework of electron-matter interaction. In transmission electron microscope imaging, when probing the thin specimen the electrons undergo the effects of elastic and inelastic scattering. The inelastic scattering is mainly due to thermal excitations of the lattice, so-called phonons. The inelastic scattering causes an electron energy loss which inherently leads to a gradual decrease (absorption) in the intensity of the elastic scattering component (elastic channel) of the electron beam [9].

The inelastic scattering on phonons is also known as thermal diffuse scattering **(TDS)**. The TDS plays a crucial role in high-resolution transmission electron microscopy **(HRTEM)** and electron diffraction since it causes the depletion in the electron elastic channel and is responsible for thermal smearing [10].

The electrons that are scattered to high scattering angles make up a significant portion of the intensity signal in the annular dark-field **(ADF)** and high-angle annular dark-field **(HAADF)** [11], that is also known as Z-contrast. The absorptive effects caused by TDS are more apparent in the ADF/HAADF since the relative value of the inelastic signal compared to the elastic signal is higher in the ADF/HAADF than in the low-scattering angle bright-field **(BF)** [12].

Various methodologies and models regarding the absorption effects exist. In this thesis, the widely used complex absorptive potentials method is compared to the more elaborate frozen phonon model coming from correlated atomic motion and Einstein model of atomic motion, respectively. [13, 14, 15, 16, 17]

Chapter 1

Fundamentals of Transmission Electron Microscopy

The field of transmission electron microscopy began in the early 1930s with the invention of the first conventional transmission electron microscope **(TEM)** by M. Knoll and E. Ruska [18]. Not much later, the invention of the scanning transmission electron microscope **(STEM)** followed [19]. It was anticipated that electron imaging could surpass conventional light microscopes, because the electron wavelength was much shorter, as was well-known thanks to L. de Broglie, who stated that every particle of matter can be assigned a so-called de Broglie wavelength [20] $\lambda = h/p$, where h is Planck constant and p is momentum. So, only a few keV of energy (therefore high momentum) is sufficient to achieve the de Broglie electron wavelength comparable to the atomic scales.

1.1 TEM Construction

Although the electron-optics development faced technical challenges, further research pushed the boundaries of TEM design, and the first commercial production began in the late 1930s by Siemens. As time passed, the (S)TEMs were further equipped with more sophisticated emission guns, electron-optical components, and high-end correctors, which today put it in a leading place in terms of spatial resolution among other instruments [1, 21]. A simplified fundamental structure of a TEM is shown in Fig. 1.1. The whole system consists of several key components, namely the electron gun, accelerator, condenser system, objective lens, specimen stage, projection system, detection chamber, and the vacuum system, which is not displayed in the figure for the sake of simplicity, and since it is mainly an external system. We now proceed in brief discussion of each of the individual components.

Electron Gun

The most commonly used electron guns are divided, by the emission process, into thermionic-emission, field-emission, or their combination. The electron beam is produced and then accelerated by a cascade of electrodes to very high energies.

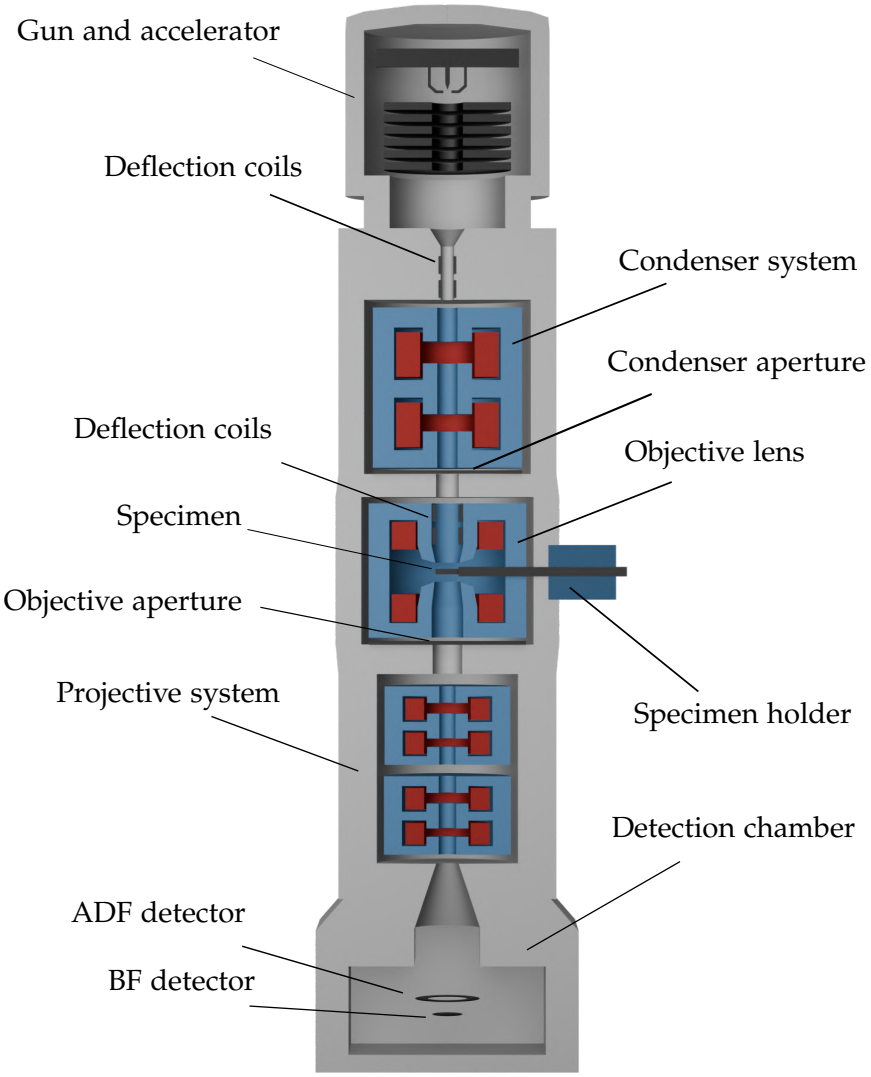

Figure 1.1: Schematics of (S)TEM.

Lenses

Lenses in electron microscopes govern the electron beam trajectory along the electron-optical column. These lenses can be either magnetic or electrostatic, but in TEM, they are predominantly magnetic and exhibit rotational symmetry. The excitation of magnetic lenses in electron microscopes is induced by passing an electric current through the coils of wire wound around a ferromagnetic core. The flowing current generates a magnetic field, thus a magnetic flux within the material of the lens. The magnetic flux is concentrated by the high-permeability core and governed through the polepieces onto the so-called gap of the lens, creating a highly localized, strong magnetic field along the electron-optical axis. The resulting magnetic field behaves as a lens and acts via the Lorentz force on the traversing electrons. The force causes electron beam rotation, which furthermore enables the focusing towards the electron-optical axis. The strength of focus then relies on the lens design and magnitude of the electric current passing through the coil's copper wires. The TEM condenser system consists of two or more magnetic condenser lenses. Condenser lenses shape the electron beam before it reaches the objective lens, and together they shape and finally illuminate the specimen. In both TEM and STEM modes, the objective lens plays the most critical role in forming

the high-resolution image, and the objective lens design aims to minimize aberrations, mainly the most influential spherical aberration [22]. The objective lens consists of upper and lower pieces; between them, in the gap, the specimen is placed. The transmitted electron beam, containing the specimen imprint, is then imaged and further magnified with (typically) four projection lenses onto the detectors.

Detectors

In TEM or STEM, various types of detectors are used to capture the signal, each utilizing slightly different contrast mechanisms. The detector choice relies on the imaging mode and the nature of the interaction between the electrons and the specimen. We may divide the primary detectors into bright-field (BF) and dark-field (DF) according to the scattering angle of the electrons, as discussed in the Introduction. While BF detectors collect unscattered electrons or the ones that have a very low scattering angle, dark-field imaging enhances contrast by capturing scattered electrons at large angles. A DF detector is located off-axis to collect scattered electrons. In TEM, the dark-field imaging can be performed using apertures placed in the back focal plane of the objective lens to let through only the electrons scattered at a high angle. On the other hand, in STEM, the acquisition of the signal is simultaneous, and the annular dark-field (ADF) and high-angle annular dark-field (HAADF) detectors consist of off-axis annular rings to collect the electrons at various angles at once. Moreover, special detectors can be used, such as energy-dispersive X-ray spectroscopy detector for X-ray signal or an electron energy loss spectrometer; these detectors process the signal originating from the inelastic interactions in the specimen.

Additional Components

The vacuum system maintains a high vacuum environment, which is necessary for the TEM operation. The vacuum quality can vary across different parts of the microscope, depending on the specific requirements of each component, e.g. cold field emission gun typically requires a very high vacuum for its operation.

Additional components as apertures, deflectors, and stigmators, are present to help control the electron beam trajectory. The apertures cut off the off-axis part of the electron beam to control the passing electron current or the electron beam angle, to reduce the off-axis aberrations effects. The deflectors are used to align the electron beam to the optical axis and, in STEM mode, are utilized to scan across the sample. The stigmator basic function is to correct the astigmatism (for example, the ellipticity) introduced by slight imperfections in the component production. For specific (S)TEM applications, geometrical aberration correctors can be mounted. Moreover, monochromators can be used to reduce the energy spread, thus chromatic aberrations.

Having established the fundamental components and instrumentation of a TEM, we will now take its setup as a given and proceed to focus exclusively on the theoretical parameters derived from it. But we will keep in mind that every theoretical parameter is linked with a function of a specific electro-optical component or their combination and may fundamentally have certain limitations. Our focus will now shift towards the theoretical aspects of image formation and electron-specimen interactions.

1.2 Basics of Imaging in TEM

In TEM, a thin sample, typically on the order of several tens of nanometers in thickness, is irradiated by an electron wave, which interacts strongly with the matter. The electron beam itself can either be transmitted without interaction or may undergo scattering, which is either elastic or inelastic. In TEM, the primary contrast is formed via elastic scattering, which occurs due to Coulomb interactions with electric charges in the sample (atomic nuclei and distribution of electrons) and preserves the electrons initial energy.

On the other hand, inelastic scattering results in electron energy losses. Additionally, the inelastic scattering is generally less localized and therefore may degrade the resolution of the image. However, the inelastic scattering processes, such as plasmon or core-loss excitations, can provide valuable spatially resolved electronic or chemical information of the sample via a technique called electron energy loss spectroscopy **(EELS)** and with high energy resolution (in tens of meV), one may observe low-loss phonon states.

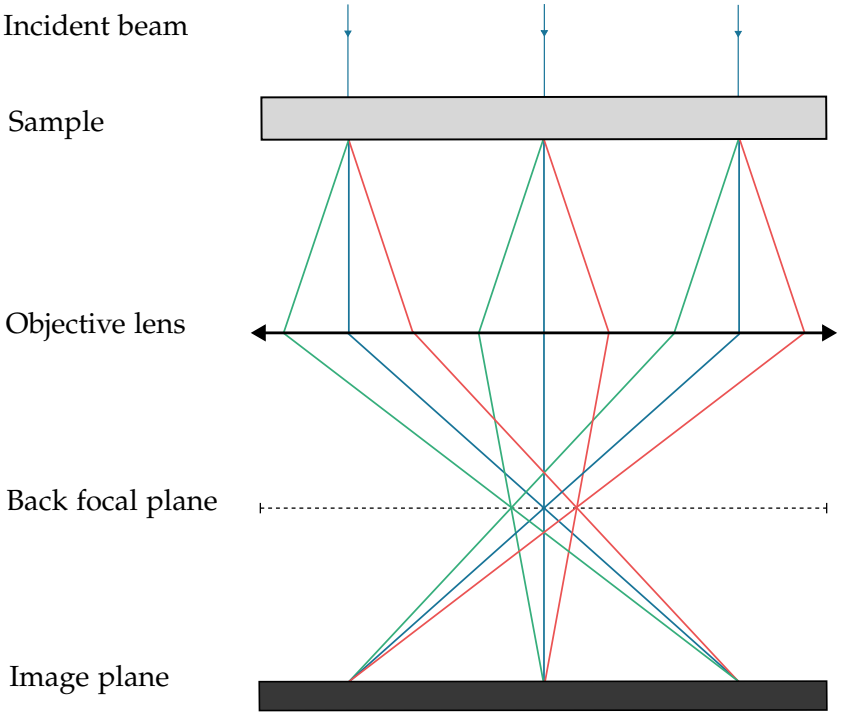

Figure 1.2: TEM imaging scheme.

In crystal samples, the scattering angles[1] depend on the crystallographic structure, and specific preferential diffraction directions, called Bragg reflections, are then apparent in the diffraction pattern. In conventional TEM, an aperture can be placed in the back focal plane to select specific diffraction spots, enabling the BF or the DF imaging. Alternatively, phase-contrast techniques, such as HRTEM, utilize the interference between scattered and unscattered electron waves to achieve atomic-resolution imaging [23].

In Fig. 1.2 scheme of TEM imaging is displayed. The incident beam is a plane wave and illuminates the sample homogeneously, we thus say the electron beam wavefront is parallel. The beam then interacts with the sample and scatters, the objective lens then

[1] Due to the high energies, the electron scattering angles in TEM are usually in the range around $1 - 200$ mrad. The signal from so-called back-scattered electrons, utilized in contrast forming in conventional low-energy scanning electron microscopy (SEM), is too weak to form an image in TEM.

focuses the scattered beam into the back focal plane and further into the image plane. In the back focal plane, the diffraction pattern can be observed because the rays diffracted at the same angle form an image in the reciprocal space. In the image plane real image of the specimen forms.

1.2.1 STEM Mode

STEM stands for Scanning Transmission Electron Microscope, a different variant of conventional TEM, i.e., STEM operates with a convergent beam of electrons instead of plane wave illumination. The convergent electron beam is focused into a spatially confined sub-nanometer electron probe, which is then scanned in a raster pattern across the specimen via the scanning coils. The scanning coil design allows for scanning in two axes across the designated specimen area and enables the collection of the signal at each pixel position.

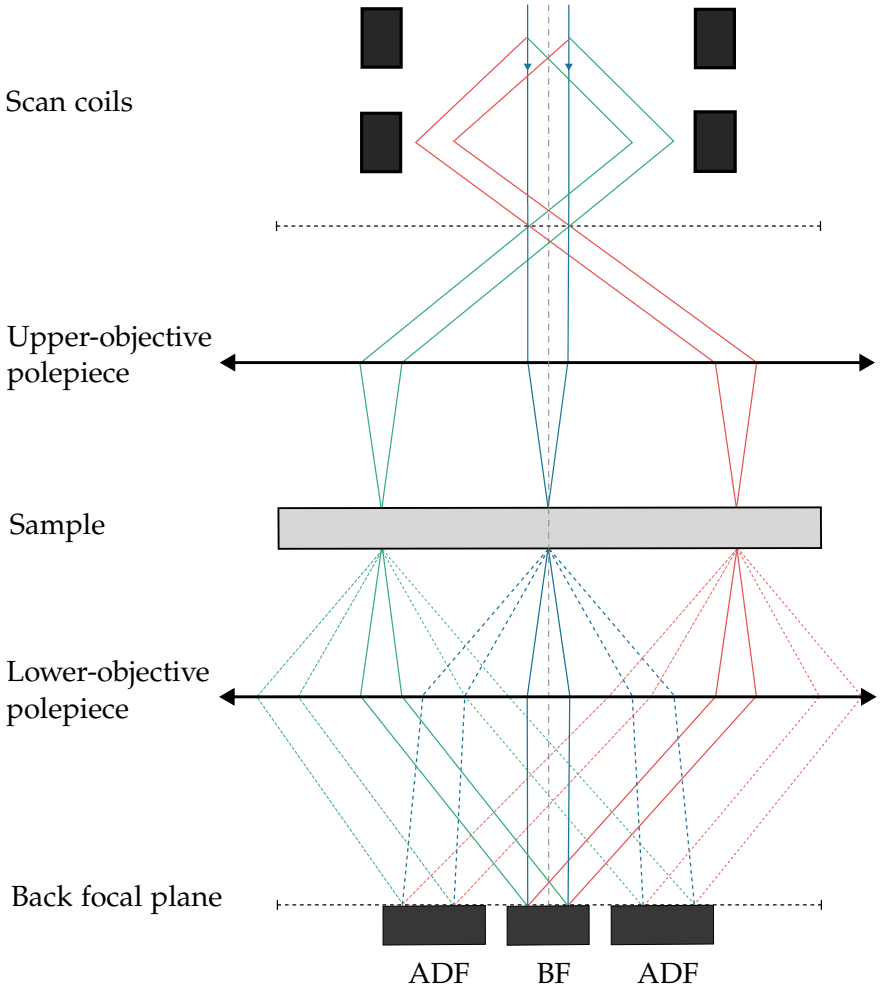

Figure 1.3: STEM imaging scheme.

The objective lens in STEM focuses the incident probe onto the sample, and the contrast is formed by detecting the transmitted or scattered electrons. The detectors, that is, the BF detector, ADF, or HAADF detector, collect the signal at various angles. As previously discussed, low-angle scattered electrons are collected to form BF images, whereas high-angle scattered electrons are captured by an ADF or HAADF detector, yielding so-called Z-contrast images, which are sensitive to the atomic number of the atoms present in

the specimen. Unlike the parallel illumination in TEM, the convergent beam in STEM allows the simultaneous acquisition of multiple signals, enabling thorough analysis of the sample. Moreover, in the STEM mode, the projection lenses may not be active, so in this mode of operation, the objective lens can transmit the electron beam directly to the detectors. The detector signal is then sent via electronics and processed in the microscope software, where the image is formed pixel by pixel in digital processing.

The resolution in STEM is primarily determined by the size of the probe and the stability of the scanning system. Modern aberration-corrected STEM instruments can achieve probe sizes smaller than 1 Å, allowing for direct imaging of individual atomic columns even in complex materials [6, 1, 12].

In Fig. 1.3, a schematic of STEM imaging is presented. The convergent probe scans pixels and can probe each position thanks to the scanning coils. The coils come in pairs to create beam shift and beam tilt; in such a way, they create a so-called pivot point in the front focal plane of the objective lens. Note that in the back focal plane of the objective lens, we can observe a diffraction pattern similar to TEM mode. However, we see that what would be one point/pixel in TEM mode is now a diffraction spot of finite diameter. One can observe these diffraction spots on pixelated detectors in a technique called convergent beam electron diffraction **(CBED)**; this fact will be utilized later on in CBED simulation.

1.3 Kinematical Theory of Electron Diffraction

In crystalline solids, the incoming electron wave scatters from the atoms in the lattice and reflects. The superposition of scattered waves from all the atoms in one or more atomic planes then results in a diffracted wave at specific angles, provided a diffraction condition is met. The resulting diffraction pattern contains information about the crystal's spatial structure and symmetries. A handful of the diffraction conditions laws have been described, with the most commonly used being Bragg's law [24]. The diffracted waves with the wavelength λ interfere destructively, or constructively, resulting in bright spots in the reciprocal (diffraction) space. We write the Bragg's law as:

$$2d \sin\theta = n\lambda, \tag{1.1}$$

where d is the distance between two atomic planes, and θ is the angle between the atomic plane and the trajectory of the reflected wave.

Although Bragg's law yields correct results, for the determination of diffracted intensity distribution, we will need to extend this theory to a more elaborate description. First, we define lattice basis vectors $\mathbf{a}_1, \mathbf{a}_2, \mathbf{a}_3$, so that each lattice vector $\mathbf{T}$ can be expressed as a linear combination of the basis vectors: $\mathbf{T} = u_1\mathbf{a}_1 + u_2\mathbf{a}_2 + u_3\mathbf{a}_3$, where $u_1, u_2, u_3 \in \mathcal{Z}$ and additionally we denote the crystallographic plane by the indices (hkl) as defined in [24]. Corresponding to real space vectors, we define reciprocal lattice basis vectors:

$$\mathbf{b}_1 = 2\pi\frac{\mathbf{a}_2 \times \mathbf{a}_3}{\mathbf{a}_1 \cdot \mathbf{a}_2 \times \mathbf{a}_3},\ \mathbf{b}_2 = 2\pi\frac{\mathbf{a}_3 \times \mathbf{a}_1}{\mathbf{a}_1 \cdot \mathbf{a}_2 \times \mathbf{a}_3},\ \mathbf{b}_3 = 2\pi\frac{\mathbf{a}_1 \times \mathbf{a}_2}{\mathbf{a}_1 \cdot \mathbf{a}_2 \times \mathbf{a}_3}.$$

And similarly as $\mathbf{T}$ in real space, we write reciprocal vector $\mathbf{G} = v_1\mathbf{b}_1 + v_2\mathbf{b}_2 + v_3\mathbf{b}_3$, where v_1, v_2, v_3 are integers.[2]

The diffraction condition then relies on the local property of the crystal $n(\mathbf{r})$, which describes the periodic electron density (and later on in Section 1.4.1 will turn into the atomic potential). We can write the function $n(\mathbf{r})$ as a Fourier series with Fourier coefficients $n_\mathbf{G}$:

$$n(\mathbf{r}) = \sum_\mathbf{G} n_\mathbf{G} e^{i\mathbf{G}\cdot\mathbf{r}}. \tag{1.2}$$

Now let's imagine an incoming wave of a wave vector $\mathbf{k}$, that scatters on the local electron density $n(\mathbf{r})$ into a wave with the wave vector $\mathbf{k}'$ and we define scattering wave vector $\mathbf{q}$ as:

$$\mathbf{q} = \mathbf{k} - \mathbf{k}'. \tag{1.3}$$

Between two points in the crystal connected with real vector $\mathbf{r}$, the incident and scattered wave experience a phase shift $e^{i\mathbf{q}\cdot\mathbf{r}}$. The amount of intensity diffracted in the direction $\mathbf{k}'$ is determined by the scattering amplitude f, which is a function of the local electron density $n(\mathbf{r})$ and the scattering wave vector $\mathbf{q}$. We integrate over the real space to account for all the contributions:

$$f(n, \mathbf{q}) = \int n(\mathbf{r}) e^{-i\mathbf{q}\cdot\mathbf{r}} d^3\mathbf{r}. \tag{1.4}$$

Furthermore, if we input the Fourier coefficients from 1.2 into 1.4 we get:

$$f(\mathbf{q}) = \sum_G \int n_\mathbf{G} e^{i(\mathbf{G}-\mathbf{q})\cdot\mathbf{r}} d^3\mathbf{r}, \tag{1.5}$$

from which we see that the diffraction condition is met for maximum in $f(\mathbf{q})$, when the reciprocal vector $\mathbf{G}$ is equal to the scattering wave vector $\mathbf{q}$, as it results in constructive interference:

$$\mathbf{q} = \mathbf{G}. \tag{1.6}$$

1.3.1 Form Factors

We now take a more generalized approach and denote the positions of the atoms in the crystal $\mathbf{r}_j$. Then we may define the so-called atomic form factor as:

$$\mathfrak{f}_j(\mathbf{q}) = \int n_j(\mathbf{r} - \mathbf{r}_j) e^{-i\mathbf{q}\cdot(\mathbf{r}-\mathbf{r}_j)} d^3\mathbf{r}, \tag{1.7}$$

where $n_j(\mathbf{r})$ is the electron density for the single atom. $\mathfrak{f}_j(\mathbf{q})$ is tightly linked to the scattering amplitude $f(\mathbf{q})$, in other words, the form factor is a scattering amplitude of one atom. Provided, the diffraction condition 1.6 is satisfied the scattering amplitude $f_\mathbf{G}$ can be expressed in terms of single cell structure factor $S_\mathbf{G}$ as $f_\mathbf{G} = NS_\mathbf{G}$, where N is the number of cells from which the diffraction is contributing. The structure factor itself is a property of the single cell and can be expressed as the following sum:

[2] The two spaces, real and reciprocal, are complementary, and in TEM we may map them in imaging mode or diffraction mode of TEM operation, respectively.

$$S_{\mathbf{G}} = \sum_j \mathrm{f}_j(\mathbf{G}) \mathrm{e}^{-\mathrm{i}\mathbf{G}\cdot\mathbf{r}_j}. \tag{1.8}$$

The definition of form factors in [24] is discussed; however, note that this form factor definition is applied for X-ray scattering (generally function n is a density of "scatterer"), but can be further recalculated to account for electron scattering by the Mott-Bethe formula [25, 26, 27]:

$$\mathrm{f}_{\mathrm{e},j}(q, Z) = \frac{me^2}{32\pi^3\hbar^2\varepsilon_0}\left(\frac{Z - \mathrm{f}_j}{q^2}\right), \tag{1.9}$$

where Z is the atomic number, q is the magnitude of scattering vector, and ε_0 is the vacuum permittivity.

1.3.2 Ewald Sphere and Laue zones

Ewald sphere construction in Fig. 1.4 is commonly used to visualize the process of diffraction; we do so in the reciprocal space (k space), and the points represent the reciprocal lattice. The incident vector $\mathbf{k}$ is defined by direction and length $|\mathbf{k}| = 2\pi/\lambda$ and is placed at the origin $\mathbf{O}$, the other end of the vector act as a center for the Ewald sphere, which then inherently has the radius $|\mathbf{k}|$. As stated in [6], any other reciprocal lattice point that lies on the Ewald sphere then satisfies the diffraction condition for scattered wave vector $\mathbf{k}'$.

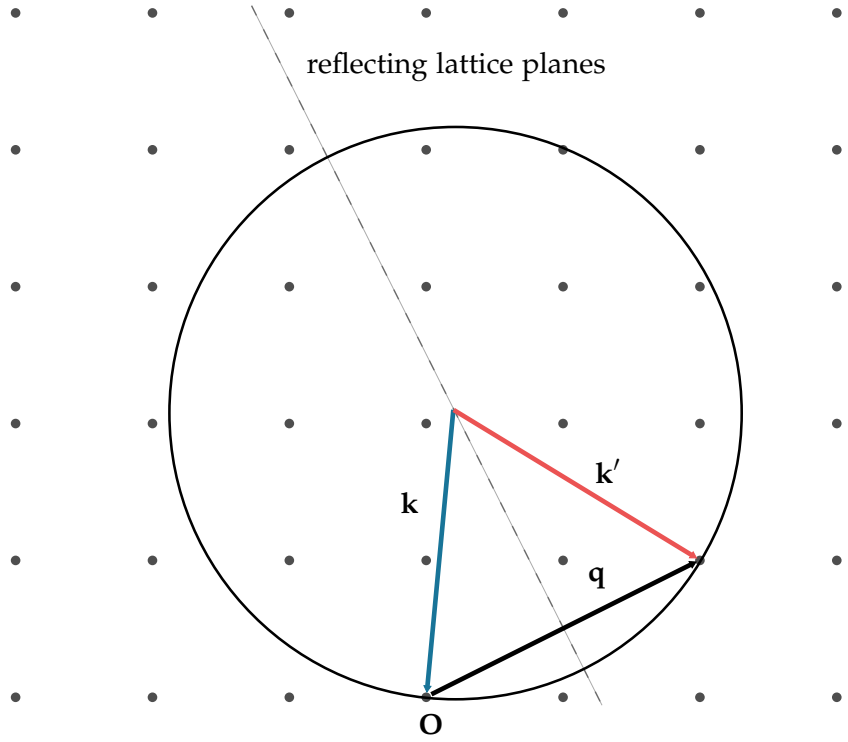

Figure 1.4: Two-dimensional representation of the general Ewald sphere construction.

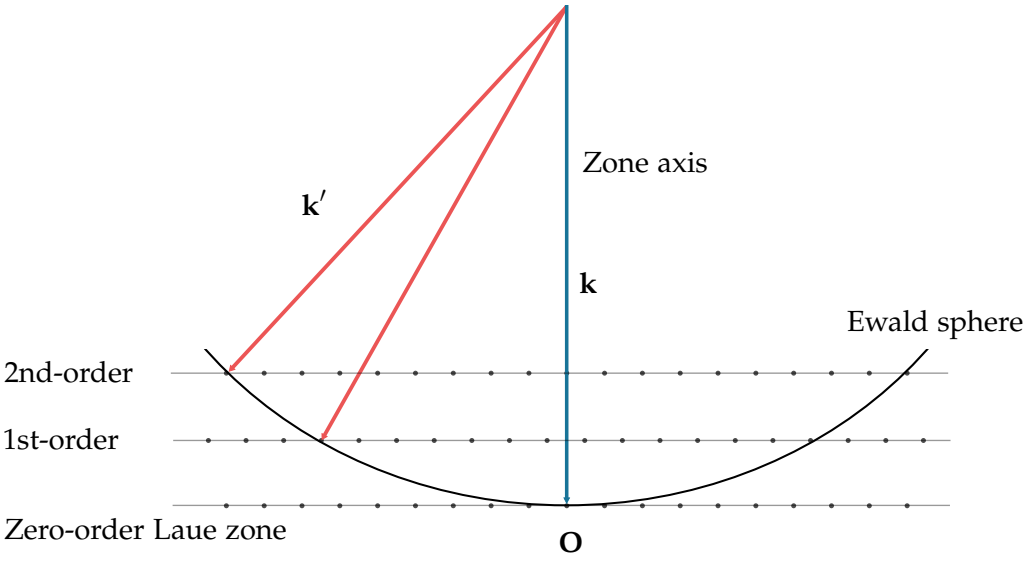

Figure 1.5: Illustrated Laue zones as in [6].

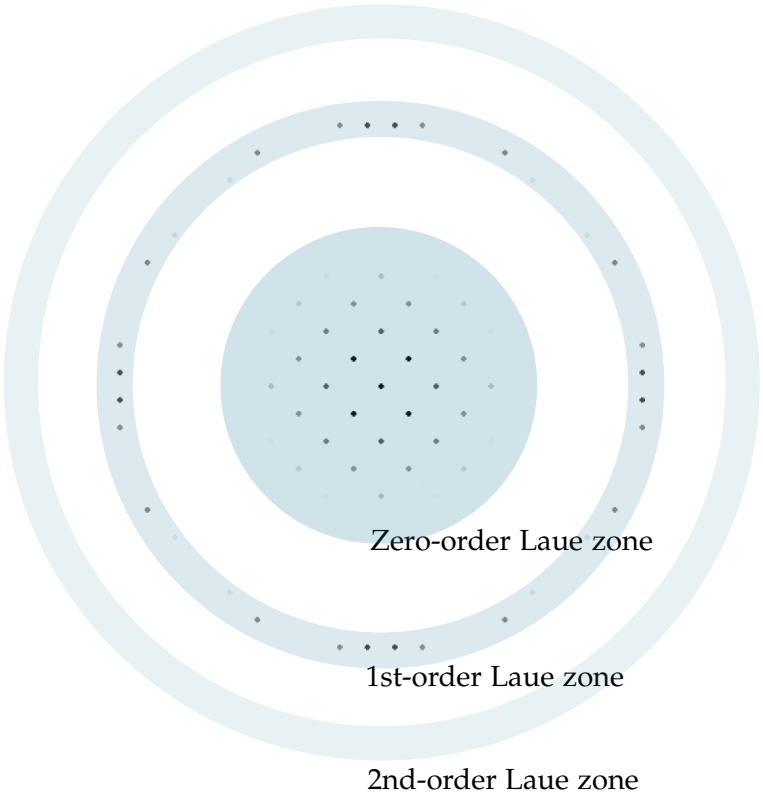

Figure 1.6: Typical electron diffraction pattern for parallel illumination in high-energy TEM, showing the diffraction Bragg spots in reciprocal space, with the gray-scale representing their relative intensity. The zero and first-order Laue zones are depicted by the blue rings. Spots in the area between those two rights then exhibit a much lower intensity compared to other Bragg spots (thus, they are not visible. Also, usually, the most intensive Bragg peaks are in zero-order and first-order Laue zone).

In case of electron diffraction in TEM, the high energy of the electrons results in a much larger radius of the Ewald sphere than in Fig. 1.4, effectively making it almost flat compared to the reciprocal distances among the reciprocal points.

The zone axis is a defined crystallographic direction, and in electron microscopy usually aligned with the direction of the electron beam, which is common to the reflecting (hkl) planes. Furthermore, if the zone-axis is parallel to the incident wave vector, for low scattering angles we see diffraction from the so-called zero-order Laue zone and for high scattering angles the Ewald sphere crosses higher-order Laue zones **(HOLZ)** depicted in Fig. 1.5. This phenomenon is then apparent in the diffraction patterns (Fig. 1.6), where we see a sudden increase in the diffraction signal intensity for high angles, which indicates HOLZ intersection.

1.4 Quantum Mechanical Theory of Scattering

The nature of electron-matter interactions, thus the scattering events, calls for a thorough description via the quantum mechanical theory and therefore also expanding the previous approach used in 1.3. We begin by introducing the fundamental equation of wave function evolution, the Schrödinger equation:

$$\mathrm{i}\hbar\frac{d}{dt}|\psi\rangle = \hat{H}|\psi\rangle, \tag{1.10}$$

where $\hbar$ is reduced Planck constant, t time, $|\psi\rangle$ the state and $\hat{H}$ is the Hamiltonian operator. Provided the potential in the Hamiltonian is time independent, the equation 1.10, can be rewritten in time independent form as:

$$E|\psi\rangle = \hat{H}|\psi\rangle, \tag{1.11}$$

where E is energy.

The Hamiltonian operator $\hat{H} = \hat{H}_0(\mathbf{p}) + \hat{H}_{\text{inter}}(V)$ will be the cornerstone of the interaction, as it generally contains the momentum of the electrons $\mathbf{p}$, and the interaction part of the system, which depend on the atomic potentials V, that affect the electron beam. We view the scattering as a transition from the initial state into the final state $|i\rangle \longrightarrow |f\rangle$. If the energy of the electron in the initial state is equal to the electron energy in the final state the interaction is elastic, otherwise it is inelastic. The transition is caused by the action of the atomic potential, which acts as a time-independent perturbation. In the elastic scattering theory as described earlier in the chapter, the negatively charged electrons in the form of plane waves in TEM mode (convergent spherical waves in STEM) interact with the electrostatic potential of the crystal, thus every atom acts as a scattering center [28, 29].

1.4.1 Scattering Amplitude and Born Approximation

It is suitable to write the probability of the elastic interaction in terms of the scattering differential cross section, which also gives us the intensity distribution. In this section we take the generalized form of scattering and simplify the problem only to a case of incident plane electron wave.

The state of the scattered electron, traversing along the z-axis, can be expressed as wave function ψ_s, which is a superposition of a wave function:

$$\psi(\mathbf{r}) = \mathrm{e}^{\mathrm{i}k_z z}, \tag{1.12}$$

and scattered wavefunction:

$$\psi_{\mathrm{sc}} = f(\mathbf{k}, \mathbf{k}')\frac{\mathrm{e}^{\mathrm{i}kr}}{r}, \tag{1.13}$$

where k_z reads as

$$k_z = \frac{2\pi}{\lambda} = \frac{2\pi\sqrt{eU(2m_0c^2 + eU)}}{hc}. \tag{1.14}$$

k_z is a relativistically corrected wave vector, λ is wavelength, e the elementary charge, U acceleration voltage, c the speed of light, m_0 electron rest mass and h the Planck constant. We can then write the superposition of the incident and scattered waves as:

$$\psi_{\mathrm{s}}(\mathbf{r}) = \mathrm{e}^{\mathrm{i}k_z z} + f(\mathbf{k}, \mathbf{k}')\frac{\mathrm{e}^{\mathrm{i}kr}}{r}, \tag{1.15}$$

where $\mathbf{r} = (x, y, z)$, $r = (x^2 + y^2 + z^2)^{1/2}$ are spatial coordinates, and $f(\mathbf{k}, \mathbf{k}') = f(\mathbf{q})$ is the scattering amplitude, and in case for single atom scattering, also a represents a form factor. Wave vector $\mathbf{q}$ is the difference between the incident and scattered wave vector $\mathbf{q} = \mathbf{k} - \mathbf{k}'$. Also, sometimes it is suitable to define angle θ as the angle between $\mathbf{k}$ and $\mathbf{k}'$, since for a spherically symmetrical potential, the $f(\mathbf{q})$ is a function of scattering angle θ. Then we can write the differential cross section as described in [28, 6]:

$$\frac{d\sigma}{d\Omega} = |f(\theta)|^2, \tag{1.16}$$

where $d\sigma/d\Omega$ is a differential scattering cross-section for scattering into the solid angle $d\Omega$.

From equations 1.15 and 1.16 it is apparent that in order to obtain results of scattered waves we need to describe the scattering amplitude $f(\mathbf{k}, \mathbf{k}')$. Previously in section 1.3 we expressed the scattering amplitude as a function of electron density, now, however, we will replace the electron density function with a different approach by inserting the atomic potential from the atoms. In general, we may write:

$$f(\mathbf{k}, \mathbf{k}') = \frac{m_0 e}{2\pi\hbar^2}\int \mathrm{e}^{-\mathrm{i}\mathbf{k}'\cdot\mathbf{r}'} V(\mathbf{r}')\psi_s(\mathbf{r}')d^3\mathbf{r}', \tag{1.17}$$

where $V(\mathbf{r})$ is then the implemented atomic potential from the atoms in the specimen. To calculate this expression is not so straightforward; that is why the Born approximation is often used for simplification of the problem, and we thus apply this approximation. We use the so-called first-order Born approximation [28]:

$$f(\mathbf{k}, \mathbf{k}') = \frac{m_0 e}{2\pi\hbar^2}\int \mathrm{e}^{-\mathrm{i}\mathbf{k}'\cdot\mathbf{r}'} V(\mathbf{r}')\mathrm{e}^{\mathrm{i}\mathbf{k}\cdot\mathbf{r}'}d^3\mathbf{r}', \tag{1.18}$$

and with the help of the previously defined relation between incident and scattered wave vectors 1.3 we can rewrite the equation as:

$$f(\mathbf{q}) = \frac{m_0 e}{2\pi\hbar^2}\int \mathrm{e}^{\mathrm{i}\mathbf{q}\cdot\mathbf{r}'} V(\mathbf{r}')d^3\mathbf{r}'. \tag{1.19}$$

This then becomes Fourier transform of the potential, which will prove to be useful when inspecting the forms of the potentials from multiple atoms in a crystal. In many

cases the scattering factors are calculated in Born approximation and then tabulated for different atomic numbers Z or alternatively use more complex models of the scattering factors such as described in [7]. Now we can take the newly acquired $f(\mathbf{q})$, and calculate the potential as inverse Fourier transform:

$$V(\mathbf{r}) = -\frac{2\pi\hbar^2}{m_0 e}\int \mathrm{e}^{\mathrm{i}\mathbf{q}\cdot\mathbf{r}} f(\mathbf{q}) d^3\mathbf{q}. \tag{1.20}$$

The effective potential of the crystal consists of individual contributions from all atoms in the crystal. To calculate the total crystal potential we sum up all the contributions as linear superpositions:

$$V_{\mathrm{tot}}(\mathbf{r}) = \sum_{j=1}^{N} V_j(\mathbf{r} - \mathbf{r}_j), \tag{1.21}$$

where $\mathbf{r}_j$ are the positions of individual atoms, from which the potential V_j contribute in position $\mathbf{r}$.

1.4.2 Phase Object Approximation

In the calculation of electrons passing through a thin specimen, the wave function phase is altered. Now once we can express the scattering effects from the specimen, we can describe the transmitted wave function in a more suitable form for the upcoming multislice method. The phase change accumulates gradually by the potentials 1.21 as the wave function passes the specimen. We can introduce a projected potential V_{proj} which is just a projection of the total potential along the trajectory of the electron beam (z-axis) resulting in 2D potential in the XY plane $V_{\mathrm{proj}}(\mathbf{R})$, where $\mathbf{R} = (x, y)$:

$$V_{\mathrm{proj}}(\mathbf{R}) = \int V_{tot}(x, y, z) dz. \tag{1.22}$$

The phase object approximation **(POA)** then expresses the transmitted wave as the initial wave function altered by this phase shift as follows:

$$\psi(\mathbf{R}) = \mathrm{e}^{\mathrm{i}\sigma V_{\mathrm{proj}}(\mathbf{R})}\psi_0(\mathbf{R}), \tag{1.23}$$

where $\sigma = \dfrac{2\pi me\lambda}{h^2}$ is the interaction parameter and $m = m_0\gamma$ relativistically corrected mass.

1.5 Multislice Method

The phase object approximation has already been introduced, and with it, we project the three-dimensional potential into two two-dimensional projection. Electron then scatters via the interaction with the projected potential.

The issue is that in probing the specimen, the interaction with only a few atomic layers already leads to multiple scattering events. Thick specimens not only modulate the phase but also the amplitude. Therefore, the previous kinematical approach no longer replicates the correct electron transmission for thick samples. We thus have to move on towards the dynamical theory of electron diffraction. The distinction in the definition of the kinematical and dynamical theories is in the number of scatterings taken into account. The kinematical theory describes only one scattering event, whereas the dynamical theory accounts for multiple scattering events. In the dynamical theory of

electron diffraction, analytically solving the problem for multiple scattering events has proved to be difficult, and new rigorous methods have to come into play [30, 7]. The dynamical theory for electron scattering was first studied by Bethe [31] in 1928, who utilized the Bloch wave representation. His theory is still used in the calculation of dynamical diffraction [32]. Furthermore, later in 1957, Cowley and Moodie presented a different method, nowadays called the multislice method [33, 7]. We will proceed to discuss and to use the multislice method, as it is more suitable and easier to implement to the calculations.

In the multislice method, we simplify the process of electron-sample interaction by splitting it into a finite number of single scattering events. In this method, we divide the sample into very thin slices, which are effectively small intervals $z + \Delta z$ along the electron trajectory (z-axis), so that we will ensure only a single (or none at all) scattering event happens in this interval, also the modulation of amplitude is negligible for very thin slices. Thus the used POA is a good approximation for very thin slices. In case the slices are not thin enough, and in the real scenario multiple scatterings happened over the incorrectly chosen slice distance, undesired discrepancies would be introduced into the calculations.

The division of the sample, in principle, inherently means division of the potential, and the potential projection 1.22 is then carried out for each of the thin slices separately. We end up with a set of two-dimensional projections of the potential separated in space by Δz, and this set then represent the whole sample, with an arbitrary thickness of the sample, that is used in TEM[3]. After having divided the space along the z-axis into slices, the electron wave function is then repeatedly propagated from one slice to another in the direction of the electron beam. As the electron wave function is propagated towards a new slice, the scattering (in this context, we will also call it transmission) occurs on the corresponding potential projection. The whole process propagation-transmission-propagation-... is then repeated until the electron wave function reaches the end of the sample [34, 35].

1.5.1 Propagation of Electron Wave Function

Let's now move on to the mathematical description of the electron propagation in the multislice method, which has been thoroughly described in [7]. As a starting point we come back to the the electron representation as an electron wave function, which should satisfy the Schrödinger equation 1.11:

$$\left(-\frac{\hbar^2}{2m}\nabla^2 - eV(\mathbf{r})\right)\psi_f(\mathbf{r}) = E\psi_f(\mathbf{r}), \tag{1.24}$$

where the Hamiltonian operator $\hat{H} = -\frac{\hbar^2}{2m}\nabla^2 - eV(\mathbf{r})$ has been inserted. The subscript in ψ_f is denoting "full" wave function, because we can then express the full wave function as a multiplication of two terms, the slowly varying $\psi(\mathbf{r})$ and a factor $e^{2\pi i z/\lambda}$, that is

[3]The sample thickness in TEM can vary from a few tens up to hundreds of nanometers, and since multiple scattering already occurs for few atomic layers, we may end up having to divide the sample in the calculation into thousands of slices.

responsible for the traversing along the z-axis:

$$\psi_f(\mathbf{r}) = \psi(\mathbf{r})\mathrm{e}^{2\pi \mathrm{i} z/\lambda}, \tag{1.25}$$

where λ is the relativistically corrected electron wavelength from 1.14. We can furthermore separate the z coordinate, from x, y and express the square of the nabla operator as $\nabla^2 = \nabla^2_{xy} + \frac{\partial^2}{\partial z^2}$, where $\nabla^2_{xy} = \frac{\partial^2}{\partial x^2} + \frac{\partial^2}{\partial y^2}$. This will help us distinguish between the in-plane components and the longitudinal components. After the substitution of the wave function 1.25 into 1.24, while the energy E is expressed as $E = 4\pi^2\hbar^2/(2m\lambda)$, we obtain the modified Schrödinger equation:

$$-\frac{\hbar^2}{2m}\left(\nabla^2_{xy} + \frac{\partial^2}{\partial z^2} + \frac{4\pi \mathrm{i}}{\lambda}\frac{\partial}{\partial z} + \frac{2meV(\mathbf{r})}{\hbar^2}\right)\psi(\mathbf{r}) = 0. \tag{1.26}$$

In an approximation the term $\frac{\partial^2\psi}{\partial z^2}$ is then neglected. This approximation, also called paraxial approximation, is valid, because for very high-energy electron the main translation happens in the z direction, thus change (the second derivative) is very small compared to the term $\frac{1}{\lambda}\frac{\partial\psi}{\partial z}$. With the use of the already introduced interaction parameter $\sigma = \frac{2\pi me\lambda}{h^2}$ we end up with an essential result featuring a first order differential equation for traversing electrons:

$$\frac{\partial\psi(\mathbf{r})}{\partial z} = \left(\frac{\mathrm{i}\lambda}{4\pi}\nabla^2_{xy} + \mathrm{i}\sigma V(\mathbf{r})\right)\psi(\mathbf{r}). \tag{1.27}$$

1.5.2 Space Discretization and Multislice Algorithm

In order to propagate the electron wave function, we have previously stated that discretization into slices is required. We thus take the equation 1.27 and plug it into a Taylor expansion in z direction $\psi(z + \Delta z)$:

$$\psi(z + \Delta z) = \psi(z) + \Delta z\frac{\partial\psi(z)}{\partial z} + \frac{1}{2!}\Delta z^2\frac{\partial^2\psi(z)}{\partial z^2} + \cdots, \tag{1.28}$$

and with substituting for Taylor expansion of an exponential function $\mathrm{e}^x = 1 + x + \frac{1}{2!}x^2 + \cdots$, which yields:

$$\psi(x, y, z + \Delta z) = \exp\left(\Delta z\frac{\mathrm{i}\lambda}{4\pi}\nabla^2_{xy}\right)\exp\left(\mathrm{i}\sigma\Delta z V(\mathbf{r})\right)\psi(x, y, z) + O(\Delta z^2), \tag{1.29}$$

where the $O(\Delta z^2)$ represents higher order expansion terms, which we are going to neglect, due to their small value. Furthermore $\Delta z V(\mathbf{r})$ will result in the projected potential 1.22 in one slice:

$$V(\mathbf{r})\Delta z = \int_z^{z+\Delta z} V(\mathbf{r})dz' = V_{\mathrm{proj}}(\mathbf{R}). \tag{1.30}$$

In

$$t(\mathbf{R}) = \exp\left(\mathrm{i}\sigma V_{\mathrm{proj}}(\mathbf{R})\right) \tag{1.31}$$

we recognize the transmission function, analogous to the one used in the POA 1.23.

Moreover, the term

$$p(\mathbf{R}, \Delta z) = \exp\left(\frac{\mathrm{i}\lambda\Delta z\nabla_{xy}^2}{4\pi}\right) \otimes \tag{1.32}$$

represents the propagation operator, where $\otimes$ is convolution, which is converted multiplication in Fourier space. The space is divided into n slices as $z_n = \sum_0^n \Delta z_j$, illustrated in Fig. 1.8, we can then denote the corresponding functions by integer index j as p_j and t_j. The wave function propagation then takes the form:

$$\psi_{j+1}(\mathbf{R}) = p_j(\mathbf{R}, \Delta z) \otimes \left(t_j(\mathbf{R})\psi_n(\mathbf{R})\right). \tag{1.33}$$

or in equivalent representation with the help of the Fourier transform FT and inverse Fourier transform FT^{-1}, which will then be particularly useful when implementing the calculation in software:

$$\psi_{j+1}(\mathbf{R}) = FT^{-1}\left[P_j(\mathbf{k})FT\left(t_j(\mathbf{R})\psi_j(\mathbf{R})\right)\right], \tag{1.34}$$

where $P_j(\mathbf{k}) = \exp\left(-\mathrm{i}\pi\lambda k^2\Delta z\right)$ is the propagator function in reciprocal space. The equation 1.34 then yields the multislice algorithm **(MSA)** solution for electron propagation through the specimen. It is also worth noting that for the indices $a < b$, the wave function ψ_a is independent of ψ_b. This effectively means that we can read out an intermediate wave function from an arbitrary sample thickness along the electron propagation. The practical realization of the specimen slicing is carried out accordingly to the specimen symmetry. In our case, the specimens will exclusively be crystalline lattice structures. Therefore, the slices should reflect the symmetries; for example, the number of equidistant slices is a whole number multiple of the atomic layers present, or another example being: eight slices per unit cell, etc. In software computations, the expression with the Fourier transforms 1.34 is, as mentioned, beneficial thanks to the speed and efficiency of the calculation method[4]. Moreover, the practical slice representation is also discretized in the xy plane, thus, the two-dimensional discrete fast Fourier transform, or FFT for short, is applied.

[4]The convolution turns into a simple multiplication in Fourier space.

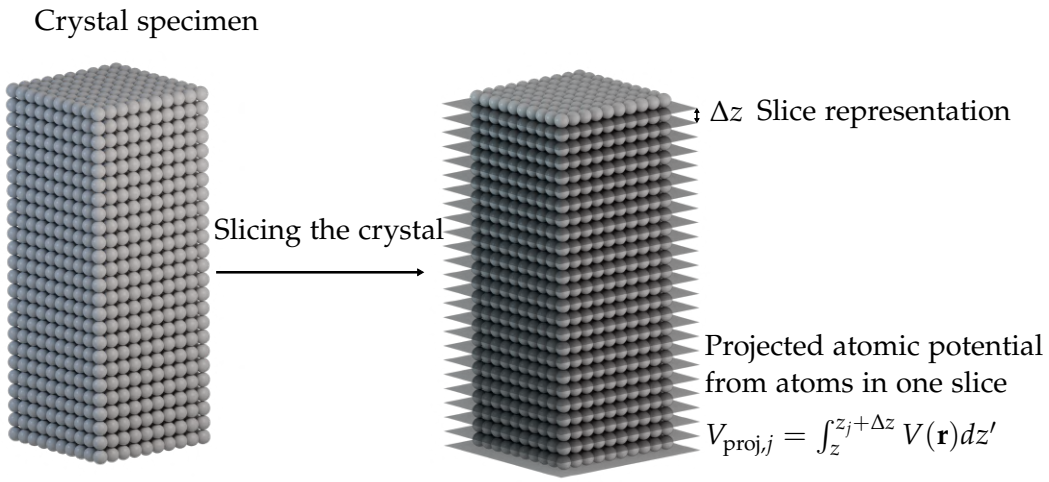

Figure 1.7: The creation of slices in the specimen, each slice then contains the projected potential of the atoms present in the particular slice.

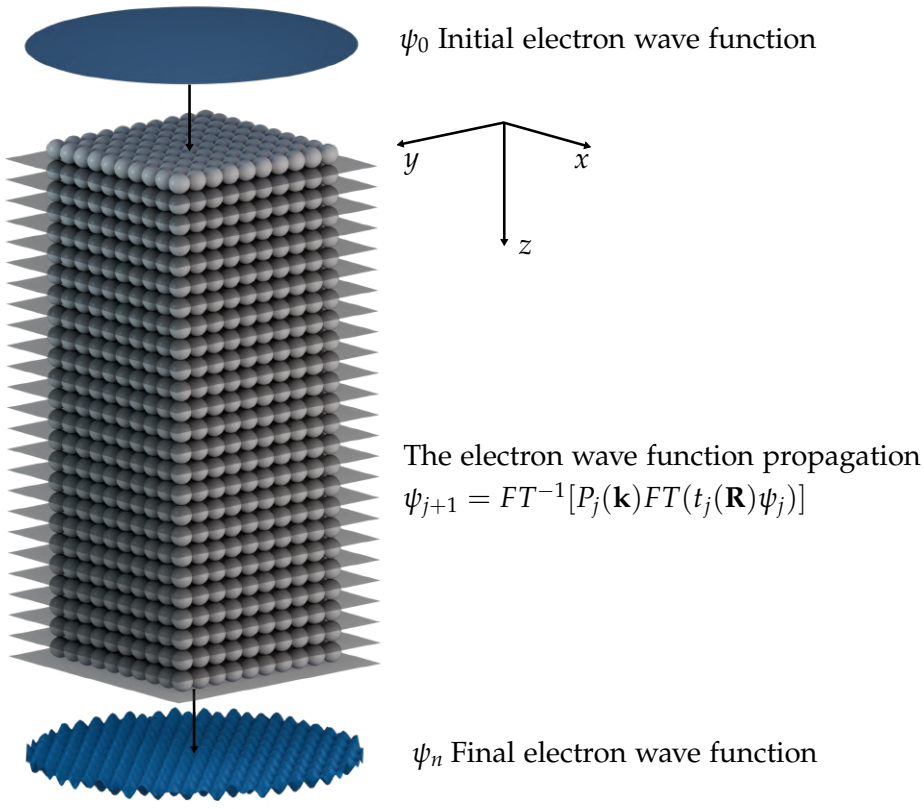

Figure 1.8: The schematics representing the multislice algorithm. We divide the specimen into thin slices and then propagate the electron wave function along the z-axis.

Chapter 2

Absorption Models

To further develop the methodologies for (S)TEM imaging modes and electron diffraction, the absorption effects have to be included [15, 36, 2]. As the electron passes through the specimen, in our case a crystal, the elastically scattered or non-scattered electrons form the main contrast in TEM, moreover in STEM, the inelastic signal can be utilized. The intensity in the so-called elastic channel is directly influenced by the losses into the inelastic component of the total intensity. Not paying attention to the absorption parts of the interaction may result in obtaining incorrect intensity distribution, and that is the reason why a good absorption model for electron scattering is needed [15, 16].

The primary losses in the Bragg-reflected electron beam are caused by exciting vibrational modes in the crystal, so-called phonons, otherwise known as the vibrations of the lattice or thermal vibrations. Other excitations such as ionization, plasmons, and magnons might be present, but for non-metal or non-magnetic specimens, these excitations are either non-existent or in our context negligible. Our primary focus is therefore on inspecting the losses in the vibrational part of the energy loss spectrum. The cornerstone of the thesis is to evaluate electron energy absorption models on phonons. But before we present three distinct absorption models, compare and evaluate them among themselves, it is convenient to further introduce the thermal diffuse scattering (TDS).

2.1 Thermal Diffuse Scattering

Generally speaking, the TDS is the background diffuse signal in diffraction patterns induced by the thermal vibrations of the atoms, which are moving around their equilibrium positions. The chaotic motion of atoms then causes the electron to be scattered seemingly randomly, which deviates from the Bragg condition, thereby making the TDS signal highly unlocalized, forming a diffuse background rather than sharp Bragg spots [37, 10, 13].

The TDS plays a crucial role in high-resolution imaging and electron diffraction. The TDS background may differ in shape, intensity, and characteristic features, such as Kikuchi lines, depending on the absorption model used. The Kikuchi lines, or Kikuchi bands, are characteristic structures on the diffraction pattern, which arise from the inelastically or diffusely scattered electrons, which are then Bragg-reflected from atomic planes and are visible outside the Bragg spots. [6, 38]

a) b)

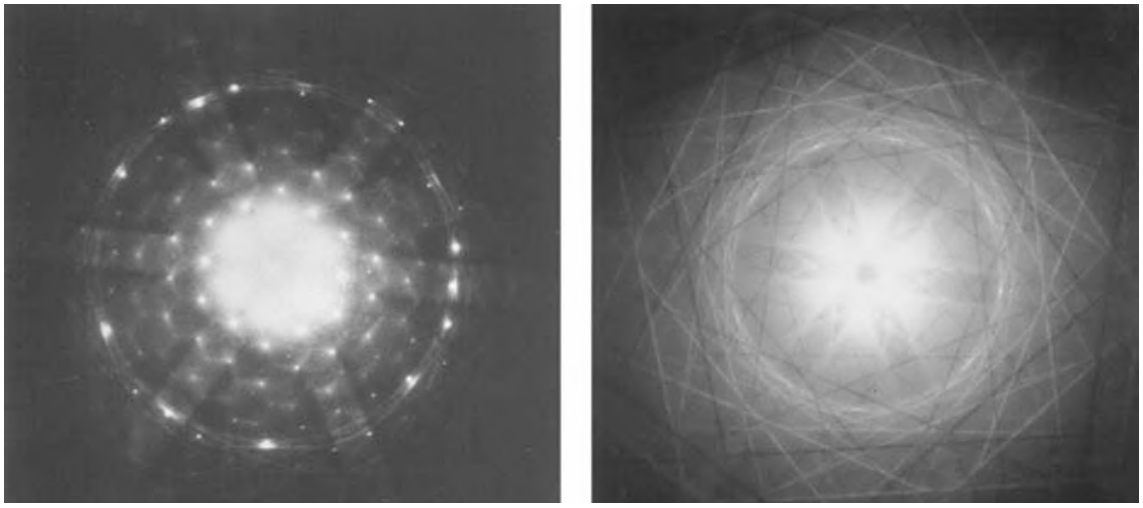

Figure 2.1: The characteristic Kikuchi bands in electron diffraction patterns of Si foils. Pattern a) shows diffraction spots of the zero- and first-order Laue zones; b) shows excess Kikuchi lines at medium angles. Reprinted from [6].

2.1.1 Debye-Waller Factor

The thermal vibrations of atoms effectively manifest as a smearing of the atomic potential around the equilibrium position of the atomic nuclei. It is valid to view the smearing as such, because in the real TEM systems, the acquisition time, to collect enough particles to form a signal, is usually much longer than the timescale on which atoms vibrate. In other words, the position of the atom around its equilibrium "averages" in time. What this means is that the atom then scatters the electron outside the Bragg spots, inherently causing a decrease in intensity in the elastic channel of the well-defined Bragg spots.

The decreased magnitude of effective potential is then described by the Debye-Waller factor **(DWF)** [6]. The DWF increases with temperature, as the atoms gain more thermal energy. DWF is also tightly linked to the mean square displacement of atoms, and arises from time-averaging of the atomic potential displacement [39]. We can express the DWF as:

$$DWF = \exp\left(-\frac{1}{3}q^2\langle \mathbf{u}^2\rangle\right), \tag{2.1}$$

where $\mathbf{u}(T)$ is the instantaneous atomic displacement, which is temperature (T) dependent, q magnitude of scattering wave vector, and $\langle\rangle$ denotes the time-averaging. Also notice the $1/3$, which implies that the atomic motion is isotropic; otherwise, generally one would have to consider all three directions in the multiplication $\mathbf{q}\cdot\mathbf{u}$, therefore we would write:

$$DWF = \exp\left(-\langle(\mathbf{q}\cdot\mathbf{u})^2\rangle\right). \tag{2.2}$$

The atomic potential $V(\mathbf{q})$ from atoms in static lattice in equilibrium is then multiplied by the DWF to introduce the thermal effects into the calculation.

2.2 Frozen Phonon Models

The first two of the absorptive models are going to be models based on the so-called frozen phonon model (method) **(FPM)**, or when directly combined with the MSA, it is called Frozen phonon multislice **(FPMS)** [3]. The frozen phonon model is a semi-classical approximative approach that incorporates electron propagation through a static lattice. Since the velocity of the impinging electron is significantly higher relative to the motion of atoms in the lattice, for the traversing electron, the atoms appear as "frozen in time"; therefore the name.

The image of the specimen in TEM consists of counting multiple electrons on the detector during the acquisition time. This behaviour is projected into the simulation via introducing a concept of so-called snapshots, i.e., static lattice configurations. The individual snapshots in FPM arise from the simulation of the atomic displacements. The snapshots represent the crystal configuration of atoms at different points in time. There is a sufficient time gap between each snapshot to emulate experimental conditions, as each traversing electron "sees" a different incoherent crystal configuration, as the electrons in real TEM would. In principle, for the electron traversing, we utilize the MSA 1.34 and propagate the electron through one configuration of the lattice, the snapshot. We repeat the process for multiple of the snapshots, each having a different atomic position distribution [3]. It is possible to then read out the wave function ψ for each snapshot, and the intensity distribution in the diffraction pattern is then the square of the wave function. Moreover, after propagating over N snapshots, the total diffraction image is expressed as an incoherent average over the number of snapshots, i.e.:

$$I_{\mathrm{FPM}} = \frac{1}{N}\sum_{n=1}^{N} |\psi(q_x, q_y)|^2, \tag{2.3}$$

where q_x, q_y are the reciprocal wave vectors. We now have to resolve the creation of the snapshot used, i.e., providing the MSA with atomic lattice arrangements from which the potential arises. In this thesis, snapshots used in the frozen phonon model are going to be of two kinds. The first kind is of snapshots corresponding to the Einstein model i.e., independent harmonic motion of atoms, further in section 2.2.1. And the second set is of snapshots with correlated atomic motion obtained via molecular dynamics **(MD)**, further discussed in detail in 2.2.2.

Note that in the FPM multislice calculation, the scattering interactions are strictly elastic, however some of the intensity is scattered outside the well-defined Bragg spots as diffuse background. These non-localized scattered waves are treated as the contribution to the inelastic signal.

2.2.1 Einstein Model

The approach in the Einstein model simplifies atomic motion by assuming that each atom vibrates independently in a harmonic potential, with the same oscillation frequency in all three directions. In practice for the calculations, this means assigning random displacements to atoms around their equilibrium positions, drawn from a Gaussian distribution whose width is tightly related to the Debye-Waller factor 2.1 or mean-square displacement, as derived from the Einstein model, we will further comment on this in 2.3.1 after discussion of the QEP theory. The atom "smearing" is then uniform and will later be apparent in the diffraction patterns in the characteristic TDS background.

2.2.2 Molecular Dynamics for Correlated Atomic Motion Model

To obtain the lattice configurations, it is necessary to simulate the motion of the lattice. For the model of correlated atomic motion, we do so by using molecular dynamics simulations in software called Large-scale Atomic/Molecular Massively Parallel Simulator, or LAMMPS for short [40]. The requirement for MD simulations may differ based upon the purpose of the simulations. For the purposes of this thesis, we need to create the crystal, i.e., a static lattice in equilibrium of the desired material. Furthermore, it is necessary to insert the inter-atomic potentials and lastly apply macroscopic conditions, such as temperature. Each atom in the simulation is assigned with position vector $\mathbf{r}$ and momentum $\mathbf{p}$, while the time domain is divided into timesteps, which are set roughly around one femtosecond apart[1].

The software then proceeds to solve classical equations of motion for all atoms, from one timestep to another, and treats the atoms as centers of mass, while the inter-atomic potential induces forces among the atoms in the lattice, and this inherently results in phononic states [17]. The equations of motion for classical particles may be expressed as:

$$\frac{d\mathbf{p}}{dt} = -\nabla V_{\mathrm{i}}(\mathbf{r}), \tag{2.4a}$$

$$\frac{d\mathbf{r}}{dt} = \frac{\mathbf{p}}{m}, \tag{2.4b}$$

where $\mathbf{p}$ is the momentum, $\mathbf{r}$ the position vector, m mass, and $\nabla V_{\mathrm{i}}(\mathbf{r})$ is the gradient of interatomic potential, which is responsible for the interatomic forces.

The initial arrangement of the atoms into the static lattice in equilibrium consists of multiples of unit cells of the crystal, and it is called the supercell. Regarding the number of atoms in the supercell, the limiting factor in the MD simulation is the computing power and memory. However, the MD computing demand scales linearly, so it is still possible to calculate supercells tens of nanometers in length, width, and height [40]. The supercell is then placed in a simulation box with periodic boundary conditions. There may be discrepancies in the macroscopic variables that may be caused by computational errors. To ensure stable macroscopic conditions of the simulations, one of the so-called statistical ensembles is applied. The ensemble used in the MD simulations, in our case, was NVT Nosé-Hoover thermostat, which maintains constant number of particles, volume, and mainly constant temperature, by controlling the kinetic energy of the system. In case the temperature is lower than the setup, it adds heat to the system, and vice versa. It is effectively realized by modifying the equations of motion 2.4 [41] :

$$\frac{d\mathbf{p}}{dt} = -\nabla V_{\mathrm{i}}(\mathbf{r}) + \kappa(t)\mathbf{p}, \tag{2.5}$$

where κ is the thermostat friction coefficient, and he value of κ changes over time (in matter of tens of timesteps) depending on the difference between actual and desired target temperature.

[1] This choice originates from the timescale of the atom movement, which is in the order of picoseconds. This means we will have a good enough sampling in the time domain.

Interatomic Potential

As stated, the governing element in the MD equations is the interatomic potential. Among the various potential models available, the Tersoff potential is a widely used potential specifically designed for covalently bonded systems, such as silicon (Si), carbon (C), and their compounds. Unlike pairwise additive potentials (e.g., Lennard-Jones), the Tersoff potential accounts for many-body interactions by adjusting bond strength based upon the local atom environment [42]. Another advantage of the Tersoff interatomic potential is that it can be easily parametrized. Moreover, machine-learned interatomic potentials represent a new way of obtaining the force fields, and combine the efficiency of classical molecular dynamics with the accuracy of quantum mechanical methods like Density Functional Theory (DFT), however for the cost of the scale of application, since machine learned potentials are usually trained to fit specific materials [43, 44, 45].

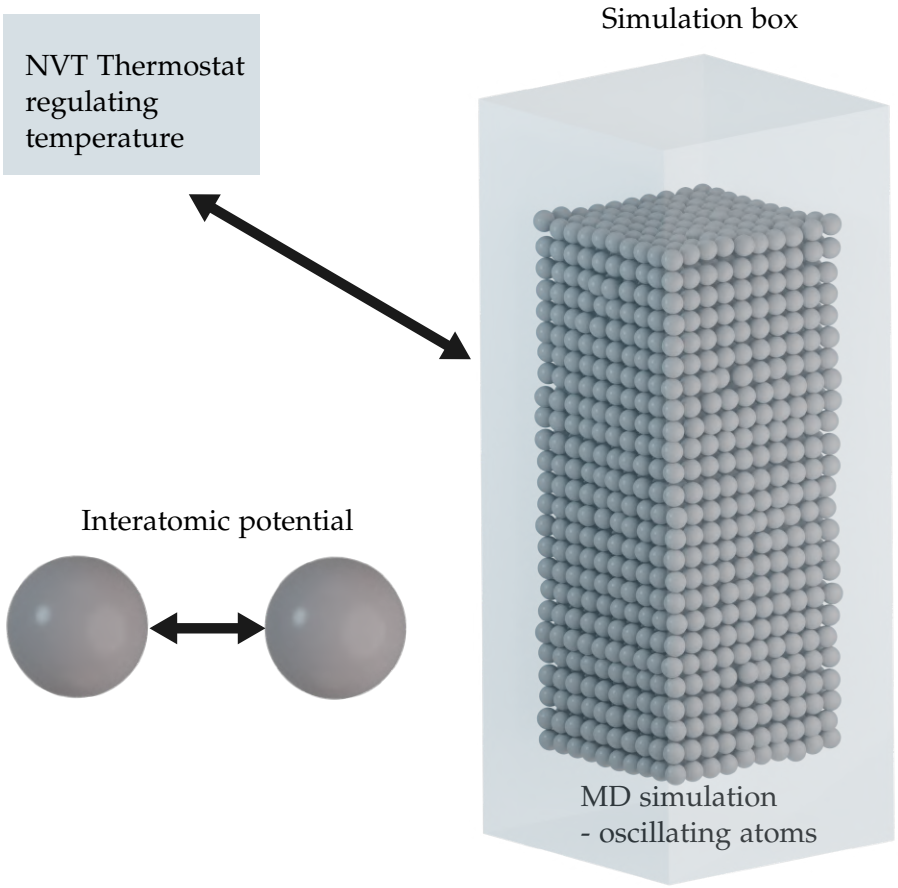

Figure 2.2: MD simulations scheme. The crystal (supercell) is contained in a well-defined simulation box with periodic boundary conditions, while the temperature inside the simulation box is being regulated by the Nosé-Hoover (NVT) thermostat. The atoms inside the crystal are governed by the Tersoff (or machine-learned deepMD) interatomic potential.

We aim to study multiple crystalline materials, including carbon in diamond lattice, silicon, and strontium titanate - STO. For the carbon and silicon, the Tersoff potential was used. In case of STO MD simulations, we used the more complex machine-learned deepMD potential [43].

2.3 Quantum Excitation of Phonons

In contrast to the semi-classical treatment by the Frozen phonon method, it is also worth viewing the system of phonon scattering from a fully quantum mechanical perspective. The theory/model of quantum excitation of phonons **(QEP)** is a many-body quantum mechanical representation of thermal electron scattering, based upon the Born-Oppenheimer approximation as presented by Forbes et al. [46]. The Born-Oppenheimer approximation states that the wave functions of nuclei and surrounding electrons can be treated separately. In reality, the mass of the electron is much smaller than that of an atomic nucleus, therefore, the approximation is valid for a broad spectrum of applications. In the theoretical framework of QEP, it is stated that the quantum mechanical calculations and the frozen phonon model calculations give the same results of intensity distributions in the diffraction pattern, and that scattering from moving lattice and quantum excitation of the crystal are equivalent. Moreover, provided both models are equivalent, it will allow us to separate the elastic and inelastic channels in the FPM calculations by utilizing the theory as stated in [46, 47]. Let's consider a fast electron impinging on a crystal. We denote $\mathbf{r}$ as the coordinate of the impinging electron, and $\mathbf{r}_j$ the particles, both nuclei and electrons, in the crystal. The Schrödinger equation of the system then is:

$$\mathrm{i}\hbar\frac{\partial\Psi(\mathbf{r},\mathbf{r}_1,\ldots,\mathbf{r}_N,t)}{\partial t} = \Bigg(-\frac{\hbar^2}{2m}\nabla^2_{\mathbf{r}} + \hat{H}_c(\mathbf{r}_1,\ldots,\mathbf{r}_N) + \\ + \hat{H}'(\mathbf{r},\mathbf{r}_1,\ldots,\mathbf{r}_N)\Bigg)\Psi(\mathbf{r},\mathbf{r}_1,\ldots,\mathbf{r}_N,t), \quad (2.6)$$

where three different parts of the total Hamiltonian are treated separately. Firstly the term $-\frac{\hbar^2}{2m}\nabla^2_{\mathbf{r}}$ is the kinetic energy of the incoming fast electron, $\hat{H}_c$ is the Hamiltonian of the particles in the crystal and lastly the $\hat{H}'$ is the interaction Hamiltonian of the incident electron to with the crystal particles [13]. Since $\hat{H}_c$ and $\hat{H}'$ are time independent, the equation 2.6 may be written via time-independent Schrödinger equation:

$$\left(-\frac{\hbar^2}{2m}\nabla^2_{\mathbf{r}} + \hat{H}_c(\tau) + \hat{H}'(\mathbf{r},\tau)\right)\Psi(\mathbf{r},\tau) = E\Psi(\mathbf{r},\tau), \quad (2.7)$$

where we defined $\tau = \mathbf{r}_1,\ldots,\mathbf{r}_N$. The wave function can then be expanded into eigenfunctions for the Hamiltonian of the crystal $\hat{H}_c$. The $a_m(\tau)$ represent mth state of the crystal (a_0 being the initial state) with eigenenergy ε_m. And the $\psi_m(\mathbf{r})$ describes the fast electron wave function after the transition $|0\rangle \rightarrow |n\rangle$. Note that the term $\psi_0(\mathbf{r})$ is an elastically scattered electron.

$$\Psi(\mathbf{r},\tau) = \sum_m a_m(\tau)\psi_m(\mathbf{r}). \quad (2.8)$$

By applying the Born-Oppenheimer approximation and separating the wave functions of the nuclei (with coordinates τ_n) and electrons in the crystal (with coordinates τ_e), we then obtain:

$$\Psi(\mathbf{r},\tau) = b(\tau_e)\sum_m a_m(\tau_n)\psi_m(\mathbf{r}). \tag{2.9}$$

Authors of QEP argue that the solution can be written in the following form [46]:

$$\Psi(\mathbf{r},\tau) = b(\tau_e)a(\tau_n)\phi(\mathbf{r},\tau_n), \tag{2.10}$$

where $a(\tau_n)$ corresponds to the subsystem of the nuclei, while a_0 is associated with the initial state of the crystal, and wave function $\phi(\mathbf{r},\tau_n)$ to the incident fast electron. After rigorous calculations [46], we obtain the intensity distribution:

$$I(\mathbf{r}) = \int |\phi(\mathbf{r},\tau_n)|^2 |a_0(\tau_n)|^2 d\tau_n, \tag{2.11}$$

and it can be shown that the intensity distribution coincides with the probability distribution $|a_0(\tau_n)|^2$. Since each incident electron may impact on a crystal, which is in different initial state a_0 (which also does not imply that it is in ground state) we assign the probability of the crystal being in a certain state with a probability distribution $P(\tau_n)$. The distribution is dependent on the temperature of the crystal, and we can express it as a function of the Debye-Waller factor. Generally though, the equation 2.11 is rewritten as:

$$I(\mathbf{r}) = \int |\phi(\mathbf{r},\tau_n)|^2 P(\tau_n) d\tau_n. \tag{2.12}$$

Furthermore, in the QEP, one can separate the elastic intensities apart from the inelastic simply by assuming the summation over initial states, which correspond to the elastic wave function $\psi_0(\mathbf{r})$, yielding only the elastic part of the scattering intensity. In other words, from the general expression for an arbitrarily scattered wave:

$$\psi_m(\mathbf{r}) = \int_V a_m^*(\tau_n)a(\tau_n)\phi(\mathbf{r},\tau_n)d\tau_n, \tag{2.13}$$

we separate the sum (average over initial states):

$$\psi_0(\mathbf{r}) = \sum_i \int_V \phi(\mathbf{r},\tau_n)P_i(\tau_n)d\tau_n, \tag{2.14}$$

where $P_i(\tau_n) = |a_i(\tau_n)|^2$.

This gives us a powerful tool for interpreting the incoherent averages of the wave functions obtained from the multislice calculations 2.3. Since both theories give numerically equivalent results, we may express the intensities in FPM (2.3) as discrete realizations of the intensities in the QEP model, therefore resulting in an expression [47]:

$$I_{\text{inelastic}} = I_{\text{total}} - I_{\text{elastic}}, \tag{2.15}$$

$$I_{\text{inelastic}} = \frac{1}{N}\sum_{n=1}^{N}|\psi(\mathbf{R})|^2 - \frac{1}{N^2}\left|\sum_{n=1}^{N}\psi(\mathbf{R})\right|^2, \tag{2.16}$$

where N is the number of snapshots, on which the multislice was conducted.

2.3.1 Statistics for Einstein model

With the help of the QEP theory, we can thereby extend the fundamental description of the Einstein model 2.2.1. In the equation 2.12, the distribution $P(\tau_n)$ may then be adjusted accordingly to the Einstein model statistics. As described in [5], we treat the atoms as independent, isotropic harmonic oscillators, and we may write the initial state coefficients $|a_0(\tau_n)|^2$, with the assumption of all the oscillators in the ground state:

$$|a_0(\tau_n)|^2 = \prod_j \prod_i |A_0(\tau_{j,i})|^2, \tag{2.17}$$

where j is the nuclei index and i denotes is indexing coordinates x, y, z. The thermally averaged $|A_0(\tau_{j,i})|^2$ then follows a distribution [5] as:

$$|A_0(\tau_{j,i})|^2 = \frac{1}{\sqrt{2\pi\sigma^2}} \mathrm{e}^{-\tau^2/2\sigma^2}, \tag{2.18}$$

where $\sigma^2 = \dfrac{\hbar}{2M\omega} \coth(\hbar\omega/2k_BT)$, furthermore M is atomic mass, ω angular frequency, k_b Boltzmann constant and T temperature. Also, $\sigma^2 = \langle\tau^2\rangle$ is the mean-squared displacement, which directly ties it together with the Debye-Waller factor [14].

2.4 Complex Absorptive Model

Finally, we will discuss the third absorption model - Complex absorptive model, following the Einstein FPM and correlated atomic motion FPM. The complex absorptive potential model as described by Yoshioka [13] views inelastic scattering as the excitation of the crystal and uses many-body quantum mechanics to describe absorption in the elastic channel due to inelastic scattering, similarly to the approach in [46]. In fact, some of the core ideas in the description of fast electron scattering in [46] were developed upon the theory of Yoshioka. However, the theories then deviate, as Yoshioka implements additional complex parts into the crystal potential, inherently resulting in an absorptive effect. First, we look at a brief historical overview of the model.

In the formalism of Yoshioka's complex absorption potentials, Hall et al. [10] states that the TDS is the leading cause of absorption and that it significantly contributes to the absorption, which strongly depends on the atomic number of the elements in the crystal. Yoshioka's theory has later been extended by Weickenmeier et al. [48], Peng et al. [27], both utilizing the absorptive scattering form factors. Further development was presented by Martin et al. [14] and Forbes et al. [9], who work in context of non-local projected potentials. Martin et al. presents and compares the complex absorptive potential model for correlated atomic motion and independent harmonic atomic motion, also known as the Einstein model, and claims that both approaches are in agreement, provided a large detector collection area. Forbes et al. shows a model for the electron energy loss spectra for multiple thermal scattering events. Forbes et al., as well as D. Van Dyck [16], show that the results of the quantum mechanical model agree well with the results of the frozen-phonon model.

The approach is similar to 2.3, starting with describing the incident fast electron scattering off a crystal with the stationary Schrödinger equation of the system:

$$\left(-\frac{\hbar^2}{2m}\nabla_{\mathbf{r}}^2 + \hat{H}_c + \hat{H}'\right)\Psi(\mathbf{r},\mathbf{r}_j,\mathbf{R}_k) = E\Psi(\mathbf{r},\mathbf{r}_j,\mathbf{R}_k), \tag{2.19}$$

while the interaction Hamiltonian $\hat{H}'$ is given by Coulomb interactions of the nuclear and electronic structure as:

$$\hat{H}' = \sum_j \frac{e^2}{4\pi\varepsilon_0|\mathbf{r}-\mathbf{r}_j|} - \sum_k \frac{Z_k e^2}{4\pi\varepsilon_0|\mathbf{r}-\mathbf{R}_k|}, \tag{2.20}$$

where Z_k is the atomic number, $\mathbf{r}_j$ denotes the coordinate of electrons in the crystal and $\mathbf{R}_k$ denotes the nuclei coordinates. The expansion of $\Psi(\mathbf{r},\mathbf{r}_j)$ (with respect to $\hat{H}_c$) can be carried out for excited states of the crystal with wave functions a_n, assuming the interaction Hamiltonian $\hat{H}'$ is small in comparison to $\hat{H}_c$. If we furthermore account for the Born-Oppenheimer approximation, we assume only the coordinates of the nuclei $\mathbf{R}_k$:

$$\Psi(\mathbf{r},\mathbf{R}_k) = \sum_n \psi_n(\mathbf{r})a_n(\mathbf{R}_k) \tag{2.21}$$

By substitution of 2.21 to 2.19 we obtain two equations, one with ψ_0 representing the elastic interaction, and one with ψ_n, representing inelastic interaction:

$$\nabla^2\psi_0 + \left(k_0^2 + \frac{2m}{\hbar^2}\hat{H}'_{00}\right)\psi_0 = \frac{2m}{\hbar^2}\sum_{m\neq 0} H'_{0m}\psi_m, \tag{2.22}$$

$$\nabla^2\psi_n + \left(k_n^2 + \frac{2m}{\hbar^2}\hat{H}'_{nm}\right)\psi_n = \frac{2m}{\hbar^2}\sum_{m\neq n} H'_{nm}\psi_m, \tag{2.23}$$

where $k_n^2 = \frac{2m}{\hbar^2}(E-E_n)$ are the scattered wave vectors. The transition $|n\rangle \longrightarrow |m\rangle$ is then treated with respect to the interaction Hamiltonian as:

$$\hat{H}'_{nm} = \int \langle n|\hat{H}'|m\rangle d\tau = \int a_n^* \hat{H}' a_m d\tau, \tag{2.24}$$

where τ is denoting the coordinates $\tau = \mathbf{R}_1,\ldots,\mathbf{R}_K$. We can further simplify equation 2.23, provided $|2m\hat{H}'_{nm}/\hbar^2| \ll k_n^2$, which is valid approximation as stated in [13]:

$$\nabla^2\psi_n + k_n^2\psi_n = \frac{2m}{\hbar^2}\hat{H}'_{n0}\psi_0, \tag{2.25}$$

The solution for 2.25 is an inelastically scattered wave, after the excitation of state $|n\rangle$:

$$\psi_n(\mathbf{r}) = -\frac{m}{2\pi\hbar^2}\int \frac{\exp\left(\mathrm{i}k_n|\mathbf{r}-\mathbf{r}'|\right)}{|\mathbf{r}-\mathbf{r}'|}\hat{H}'_{n0}(\mathbf{r}')\psi_0(\mathbf{r}')d\mathbf{r}'. \tag{2.26}$$

By substitution of the equation 2.26 into 2.22 we obtain:

$$\nabla^2\psi_0 + \left(k_0^2 - \frac{2m}{\hbar^2}\hat{H}'_{00}\right)\psi_0 + \frac{2m}{\hbar}\int A(\mathbf{r},\mathbf{r}')\psi_0(\mathbf{r}')d\mathbf{r}' = 0, \tag{2.27}$$

where

$$A(\mathbf{r},\mathbf{r}') = -\frac{m}{2\pi\hbar^2}\sum_{n\neq 0}\hat{H}'_{0n}(\mathbf{r})\hat{H}'_{n0}(\mathbf{r}')\frac{\exp(\mathrm{i}k_n|\mathbf{r}-\mathbf{r}'|)}{|\mathbf{r}-\mathbf{r}'|} \tag{2.28}$$

is a nonlocal potential representation. Further definition from [2] converts it into hermitian nonlocal absorptive potential $W(\mathbf{r},\mathbf{r}') = \mathrm{i}[A(\mathbf{r},\mathbf{r}') - A^*(\mathbf{r},\mathbf{r}')]$. In multislice, we also need the potential to be projected into a two-dimensional plane; we do so with the following integration:

$$W(\mathbf{R},\mathbf{R}') = \frac{1}{\Delta z}\int_z^{z+\Delta z}\int_z^{z+\Delta z} \mathrm{e}^{-\mathrm{i}kz} W(\mathbf{r},\mathbf{r}')\mathrm{e}^{\mathrm{i}kz'}\,dz dz'. \tag{2.29}$$

It is also stated that in case of a large enough detector (large collection angle), we may further translate the nonlocal absorptive potential into local absorptive potential V' via local approximation [2]:

$$W(\mathbf{R},\mathbf{R}') \approx 2V'(\mathbf{R})\delta(\mathbf{R}-\mathbf{R}'). \tag{2.30}$$

In the treatment of [48, 27], the complex absorptive potentials V' are then used alongside the real part of the potential. Furthermore, they can be implemented and parametrized into so-called complex absorptive form factors, which are a direct extension of the regular form factors. The multislice algorithm software [34], which we use in this thesis, utilizes this theory of absorptive form factors from [48] in optional absorptive calculations.

In Fig. 2.3 we see an illustrative depiction of the shape of the components for complex absorptive potential. The projected potential comes from a slice as used in diamond calculations.

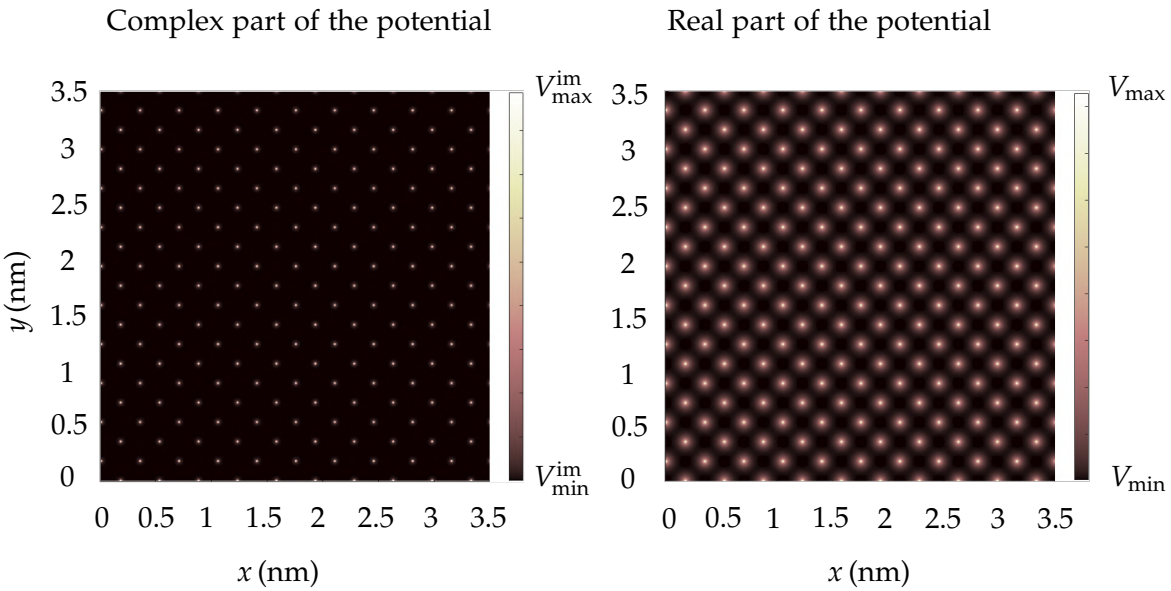

Figure 2.3: The components of the projected local potential $V'(\mathbf{R})$ in slice (slice which contains atoms) in arbitrary units. The potentials come from the calculations for diamond 3.1.

Chapter 3

Calculations and Results

In the third chapter, a detailed overview of the extensive calculations and simulations will be presented. We begin with the specific implementation of molecular dynamics simulations (2.2.2) and proceed to the multislice method (1.34) [49], while the absorption models will be applied for each crystal sample. The three models as presented in chapter 2 are the frozen phonon model for the Einstein model of atomic motion, then the FPM for correlated atomic motion with atom motion implemented as snapshots from MD simulations, and lastly the Complex absorptive model.

We aim to obtain the intensity distribution in diffraction patterns, mainly the elastic component of the intensity, which is depleted due to the losses into the inelastic channel. The frozen phonon models also offer the possibility of extracting the inelastic part of the signal by subtracting the elastic component from the total intensity, yielding the shape of the TDS background. Furthermore, the total intensity, more precisely, the square of the absolute value of the total wave function, is the value measured on the detector. In the frozen phonon models, the diffraction pattern is obtained via thermal averaging over the correlated atomic motion snapshots, or configuration variants in the case of the Einstein model.

The quality of the FPM diffraction pattern simulation is then determined by the residual TDS noise in the elastic channel, since in theory, for an infinite number of snapshots/variants, the elastic channel should contain the Bragg peaks only. Therefore, the more snapshots/variants we use, the lower the noise should be and the more precise the FPM diffraction patterns are.

The frozen phonon model with correlated atomic motion is expected to be the most exact in comparison to experiment, in terms of intensity distribution and characteristic features. Primarily because of its capability to realistically represent the phonon modes. The main limitation being the quality of the interatomic potential used. [16, 50, 17]

We then begin the analysis of the diffraction pattern and compare the depleted elastic components of the models, which will give us an idea about the validity and potential discrepancies with experiments, in certain use cases. But before we dive into the evaluation and comparison of the models, let's define the crystalline materials upon which the calculations are carried out, and also their resulting lattice configurations from MD.

3.1 Crystal Materials and Molecular Dynamics

The definition of the crystals took place in the LAMMPS software. Previously, we discussed the MD simulations for the FPM with correlated atomic motion, which were carried out in LAMMPS. But the functionality of the software also allowed us to also create just one snapshot of a static lattice configuration in the equilibrium, for the use in the Einstein model and complex absorptive model. Three of the crystal samples created, namely carbon atoms in diamond lattice - Diamond, strontium titanate $SrTiO_3$ - called STO, and silicon in diamond lattice - Si.

Each of the crystals is defined by a unit cell with specifically set lattice parameters, then the unit cell is repeated to obtain the desired dimensions of the supercell. We have to be cautious in choosing the dimensions, since we are limited by the memory and computational power of the machines. Also, the machine-learned potentials for STO are much more computationally demanding than the simpler Tersoff variants for diamond and silicon, thus resulting in a smaller supercell. We now proceed to describe each crystal in detail.

3.1.1 Diamond

The choice for the carbon (C) atoms in diamond lattice was made based on the idea of testing the absorption models on relatively light atoms (atomic mass 12.011 u[1]), and later to put it in contrast with the results from the STO crystal containing heavy elements. The diamond crystal dimensions are 3.5 nm × 3.5 nm × 50 nm and the lattice parameter of the face-centered cubic unit cell is set to 0.35724 nm [24] (slightly adjusted for convenient thermal relaxation). The supercell is oriented in such way so that the xy plane face is (001) surface, depicted in Fig. 3.1. The structure is simple and trivial to define, also the interatomic potential for diamond, which was a carbon (C-C) Tersoff potential, is accessible and easy to implement.

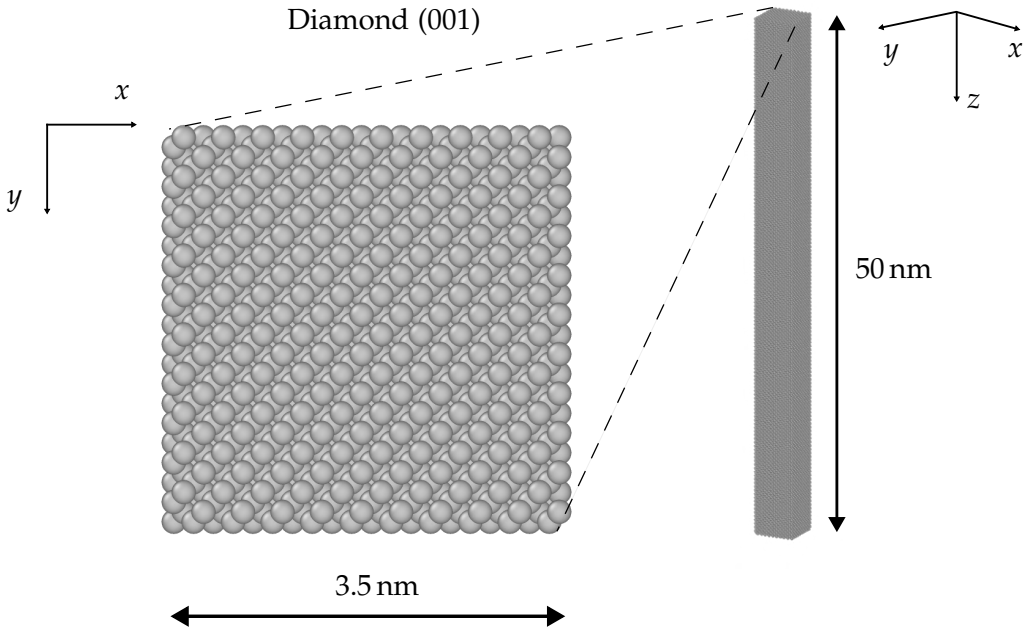

Figure 3.1: The supercell of diamond, top view (on the left), side view (on the right).

[1]The atomic mass unit is defined as u = 1.660539066 × 10^{-27} kg

Concerning the MD, the process consisted of letting the MD simulation run for a couple of thousand timesteps (one timestep is set to 1 fs) from the starting point, which was the lattice in equilibrium. In this way, we ensure that the crystal has enough time to thermally relax. The crystal was kept at 300 K via NVT thermostat, and after the thermal relaxation, snapshots are read out every 1000 timesteps. The MD simulations yielded total of 100 snapshots, which are stored in .xyz data file, containing coordinates of all the atoms, in every snapshot configuration. In the Einstein model 50 variants were used, since the noise threshold in diffraction patterns was determined to be low enough compared to the main Bragg peak intensity.

3.1.2 Strontium Titanate

As stated, the heavy elements of STO will represent a testing sample for the models in contrast to the light carbon atoms in diamond. Moreover, the STO exhibits anisotropic vibrations, which is another variable in the absorption model procedure and the anisotropy may result in significat differences in the models (for example, the basic form of the Einstein model calculates with isotropic displacements).

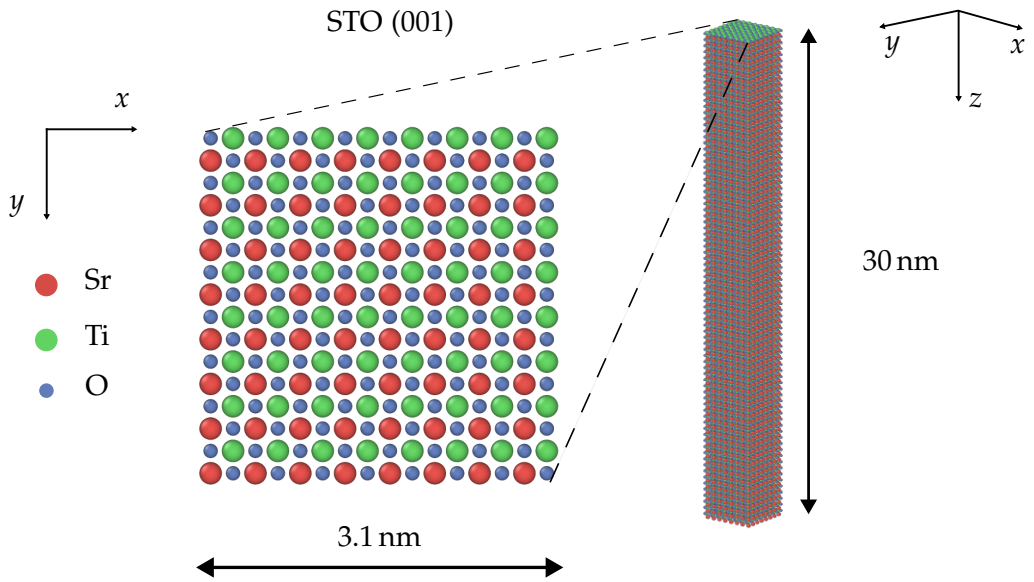

Figure 3.2: The supercell of strontium titanate, top view (on the left), side view (on the right).

We further define the crystal of STO; chemically $SrTiO_3$, namely strontium (Sr, atomic mass 87.62 u), titanium (Ti, atomic mass 47.867 u) and oxygen (O, atomic mass 15.999 u) with cubic unit cell lattice parameter 0.3905 nm [51] (slightly adjusted for convenient thermal relaxation). Due to the complexity of MD calculations with the machine-learned deepMD interatomic potential, the size of the supercell needs to be reasonably small. Otherwise, the calculations would be time-consuming, due to the sheer computational demand. The supercell dimensions are 3.1 nm $\times$ 3.1 nm $\times$ 30 nm, with the supercell face oriented in (001). The structure is further shown in Fig. 3.2.

The MD simulation process was analogous to the one presented in 3.1.1, i.e., temperature of 300 K with thermal relaxation of the crystal. The only difference in the process was in the use of the deepMD interatomic potential for STO. The MD simulation then resulted

in obtaining 100 snapshots in .xyz files. The variants in the Einstein model were later set to 100 as well.

3.1.3 Silicon

The Silicon (Si) crystal is the only one of the crystals to be probed by a convergent beam in the convergent beam electron diffraction (CBED). It is because the aim is to compare the model characteristic features to experimental data, and Si CBED measurements happen to be very common and accessible. However, the experiments are rarely carried out on very thin samples (below 50 nm), thus the simulations require the construction of a larger supercell than it was in the previous two crystals. Here, the computational demand is not as high as for STO, because we once again use Tersoff potential, now in (Si-Si) variant.

The construction of FCC silicon (atomic mass - 28.0855 u) crystal with lattice parameter 0.5430 nm [24], was performed. The dimensions therefore are: 6.2 nm $\times$ 6.2 nm $\times$ 85 nm oriented so that the face is in (111) orientation[2] Fig. 3.3. After an analogous process to diamond, once again, 100 snapshots are the result of the MD simulations, and later, we set 50 atomic variants for the Einstein model.

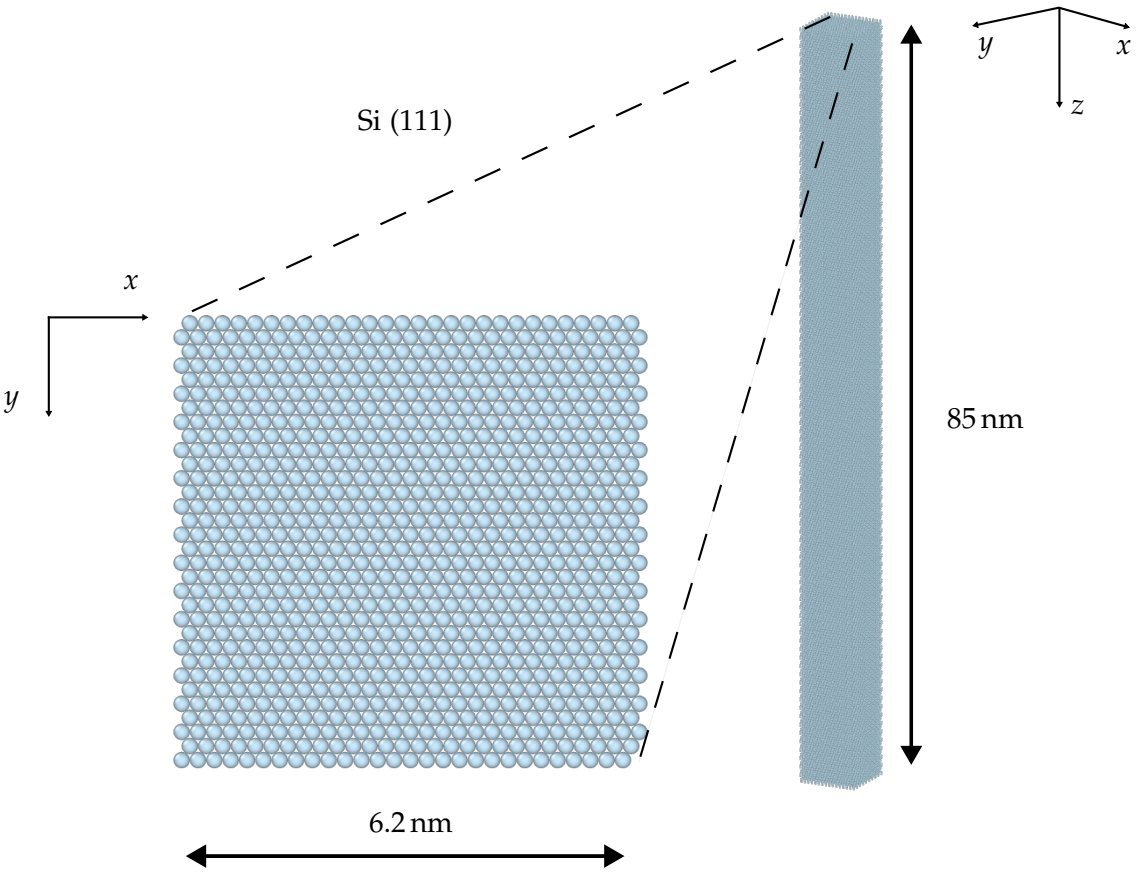

Figure 3.3: The supercell of Si, top view (on the left), side view (on the right). Note that, unlike in previous crystals, the orientation of the face is (111).

[2]The (111) orientation was chosen because of the comparison with Si(111) CBED experiments

3.2 Multislice Calculations

In this section, the process of multislice calculations is discussed. The main tool in this case is the Dr. Probe software [34]. This software not only implements the MSA as described in 1.34, but also contains multiple functionalities that will come in useful. For the case of the correlated atomic motion model, the distribution of atoms is obtained exclusively from the previous LAMMPS MD simulations, and Dr. Probe then only projects the potential from the atoms present. However, a special functionality exists for the Einstein model, i.e., independent harmonic motion of atoms, which enables the generation of atomic variants (completely analogous to snapshots in MD). These atomic variants are generated with the user's specification of Debye-Waller factors, which are element-specific. Moreover, there is also a possibility of applying the complex absorptive potentials in the form of [48]. In contrast to the Einstein model or the correlated atomic model, the complex absorptive model consists of only one simple propagation through the static lattice in equilibrium, but also requires the specification of DWF. The single propagation then results in an elastic channel intensity distribution, which is decreased by the effect of inelastic scattering. Also, unlike in the FPM, in the complex absorptive model, the TDS distribution cannot be obtained.

Firstly, by an own code in Python, the .xyz atomic configuration data from LAMMPS were converted into .cel files so that the Dr. Probe software may read them. The .cel files are software-specific definition of atomic coordinates in the supercell, which is then divided into slices. For each case of the model and for all the materials in question, potential projections in individual slices were created, accordingly to the model in use. Namely, we define the x-y resolution of the simulation (discretization of the supercell in xy plane) and then we define the number of slices (discretization of the supercell in z direction). To represent the potential and beam wave functions, we have used numerical grids of 640 px$\times$640 px for all materials. The potentials are then projected via software binary function "celslc" in slices and then stored as so-called .sli data files. The .sli files are in many cases very large.[3] Once all the .sli files containing the two-dimensional projected potentials are calculated, the multislice algorithm may take place.

The parameters of the simulations are controlled by so-called parameter files .prm, where the TEM setup is defined, i.e., accelerating voltage, detector area, beam tilt, and aberrations. The aberrations are in our case set to zero, we use an aberration-free system to selectively highlight the effects that are introduced by the TDS. Further in STEM mode, we define the probe position and convergence angle (otherwise we use TEM parallel illumination, where the convergence angle is set close to zero and the probe position is thus irrelevant). The acceleration voltage was set to 300 kV, except for Si CBED calculations, where it was set to 100 kV. The "msa" function then works with uploaded .sli files into the memory, whilst applying the TEM parameters from the .prm file. The wave function, which has intensity normalized to one, is propagated from slice to slice, where it is transmitted, as described in 1.34. The results consist of wave function values in binary data files (in numbers float32/64) in a chain containing a pair of numbers: real and complex for each pixel. These files are further analysed (the FPM according to 2.3) in MATLAB/Python, yielding intensity distributions in diffraction patterns.

[3] The file size is determined by x resolution $\times$ y resolution $\times$ 32/64 bits (the data limit for one pixel, 64bit is for the case the numbers are double-precision floating-point format) $\times$ number of slices. And in the process of electron propagation, all these slices are then loaded into the RAM memory, it is therefore recommended to choose a suitable sampling, not to exceed the memory capacity of the computing device.

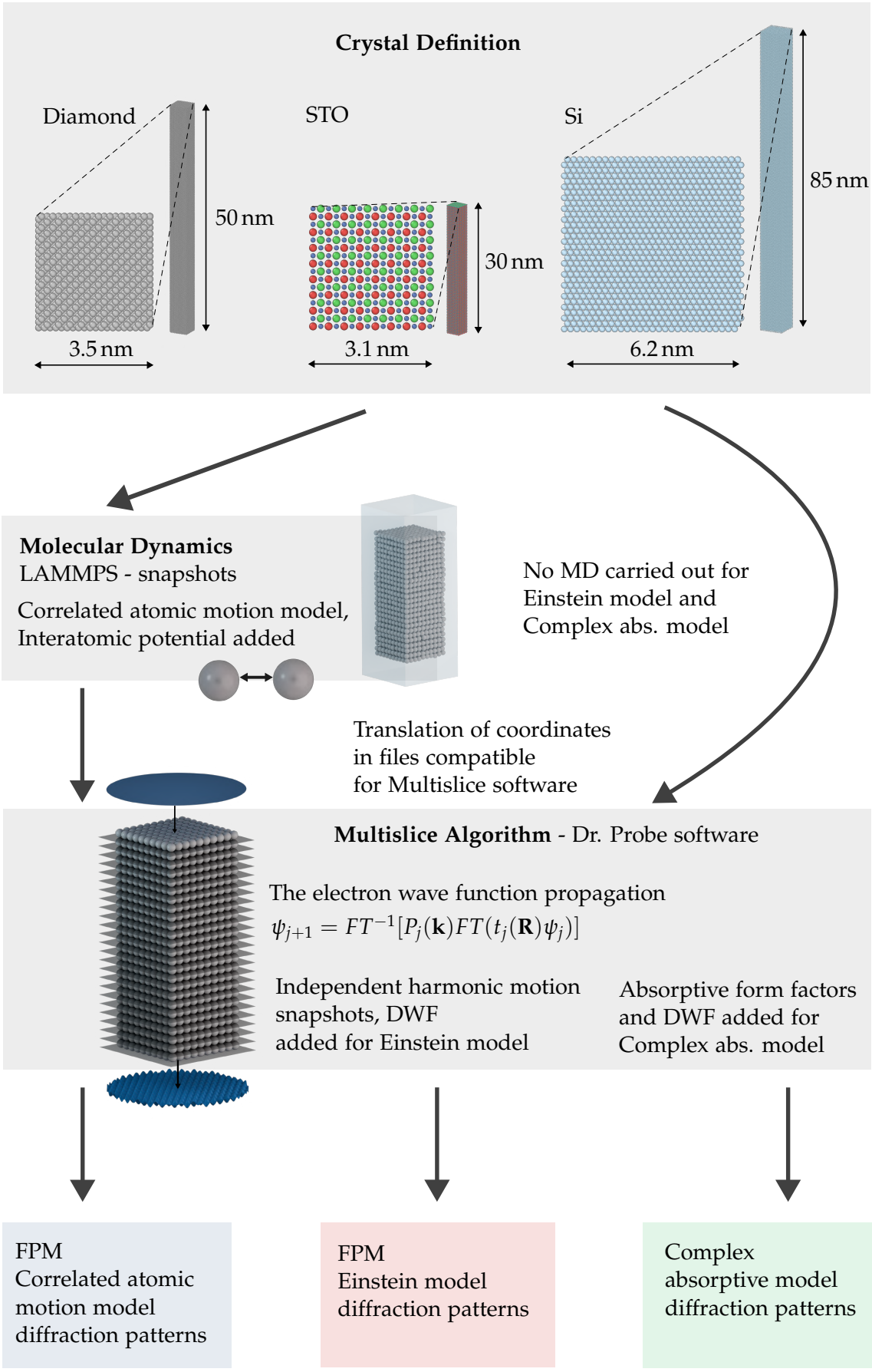

Figure 3.4: Scheme of the calculation processes. The corresponding calculations were carried out for all three materials, that is, 3 models $\times$ 3 materials.

3.3 Resulting Diffraction Patterns

We now show and analyze the results of the calculation processes. First, we show the diffraction patterns from the inspection of the three materials, then we proceed into more deeper analysis of the intensity profiles. There are seven possible relevant diffraction pattern outputs for each material, that is, the total FPM intensity of correlated atomic motion model and Einstein model (2), inelastic intensity channel (TDS) from both of the model (2), elastic channel for both frozen phonon models (2), and lastly the complex absorptive potential calculation, which yields only the elastic channel intensity (1). Special attention then will be put on the total intensity in CBED patterns from Si, which will be compared by characteristic features with experiment.

We start by showing the set of diffraction pattern outputs for the diamond crystal, a total of five (without the TDS). The signals displayed are total intensity and elastic channel; the TDS is then apparent by observing the background of the total intensity pattern outside the one-pixel Bragg spots. In Diamond and STO, we are then interested in the depleted elastic channel, which will later be compared among all the models. And to compare the features of diffractions with experimental data, we will use and show the total intensity (representing detector measurements) in Si CBED patterns.

3.3.1 Diamond Results

In Figs. 3.5-3.6 is the elastic channel from the complex absorptive model and FPM, and in Fig. 3.7 we see the total intensity FPM diffraction patterns.

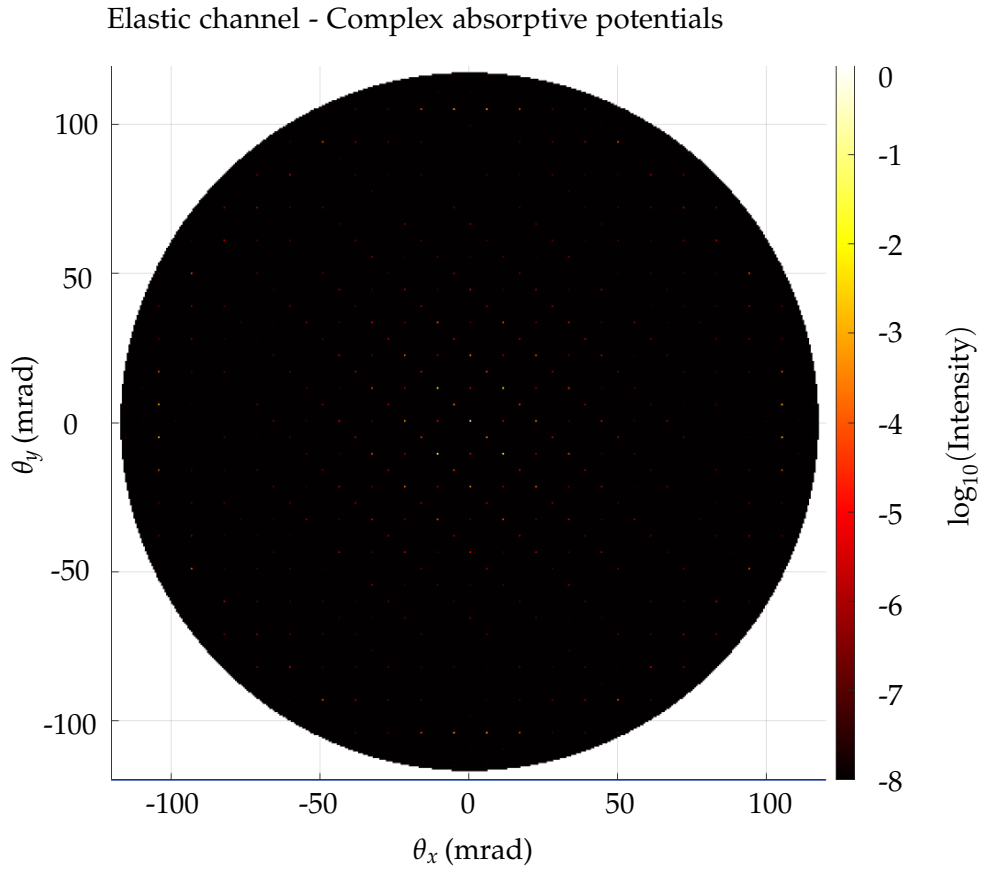

Figure 3.5: Diffraction pattern, elastic channel of complex absorptive potential model for diamond with thickness $t = 50\,\text{nm}$, and electron accelerating voltage $U = 300\,\text{kV}$.

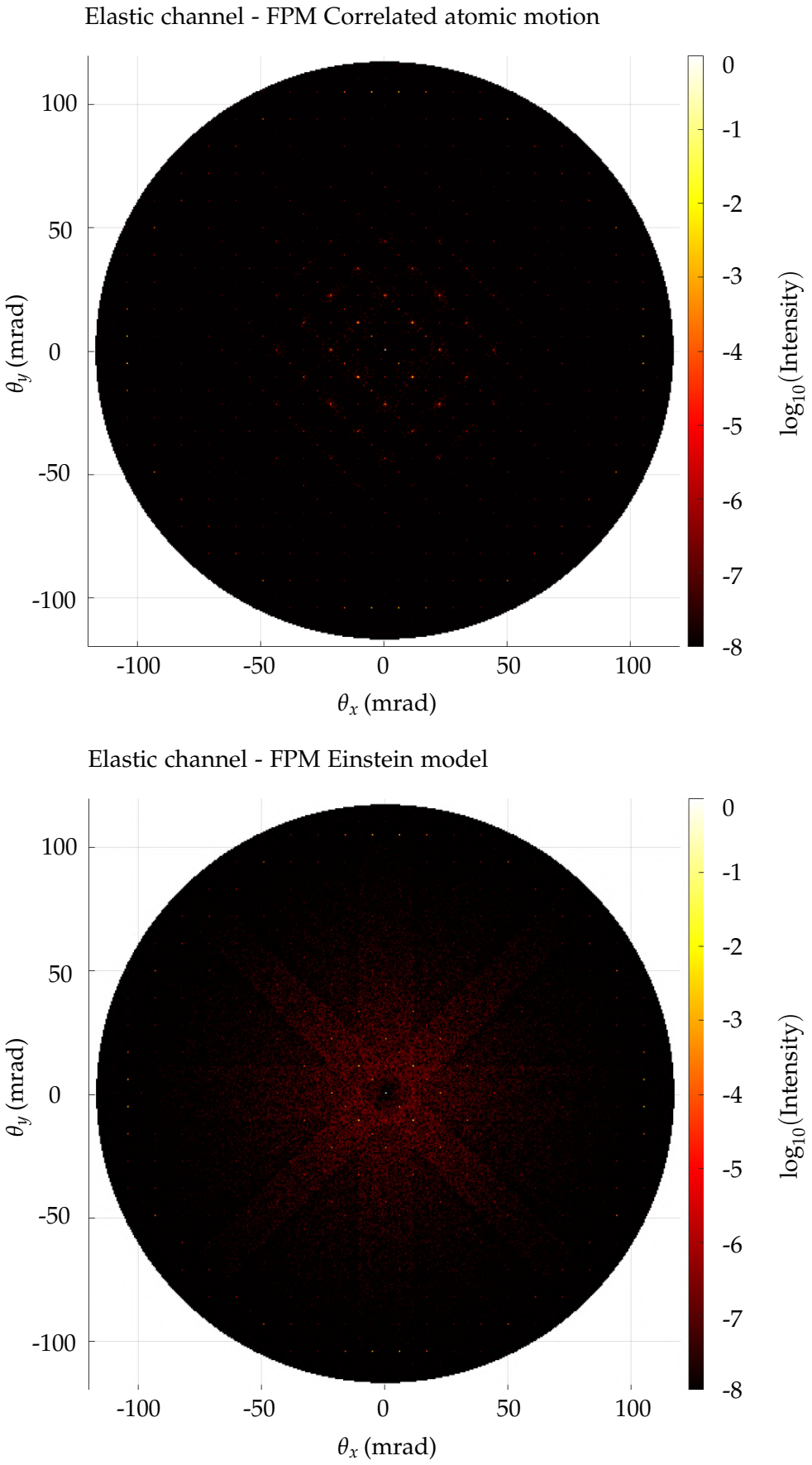

Figure 3.6: Diffraction patterns, elastic channel of frozen phonon models for diamond with thickness $t = 50\,\text{nm}$, and electron accelerating voltage $U = 300\,\text{kV}$.

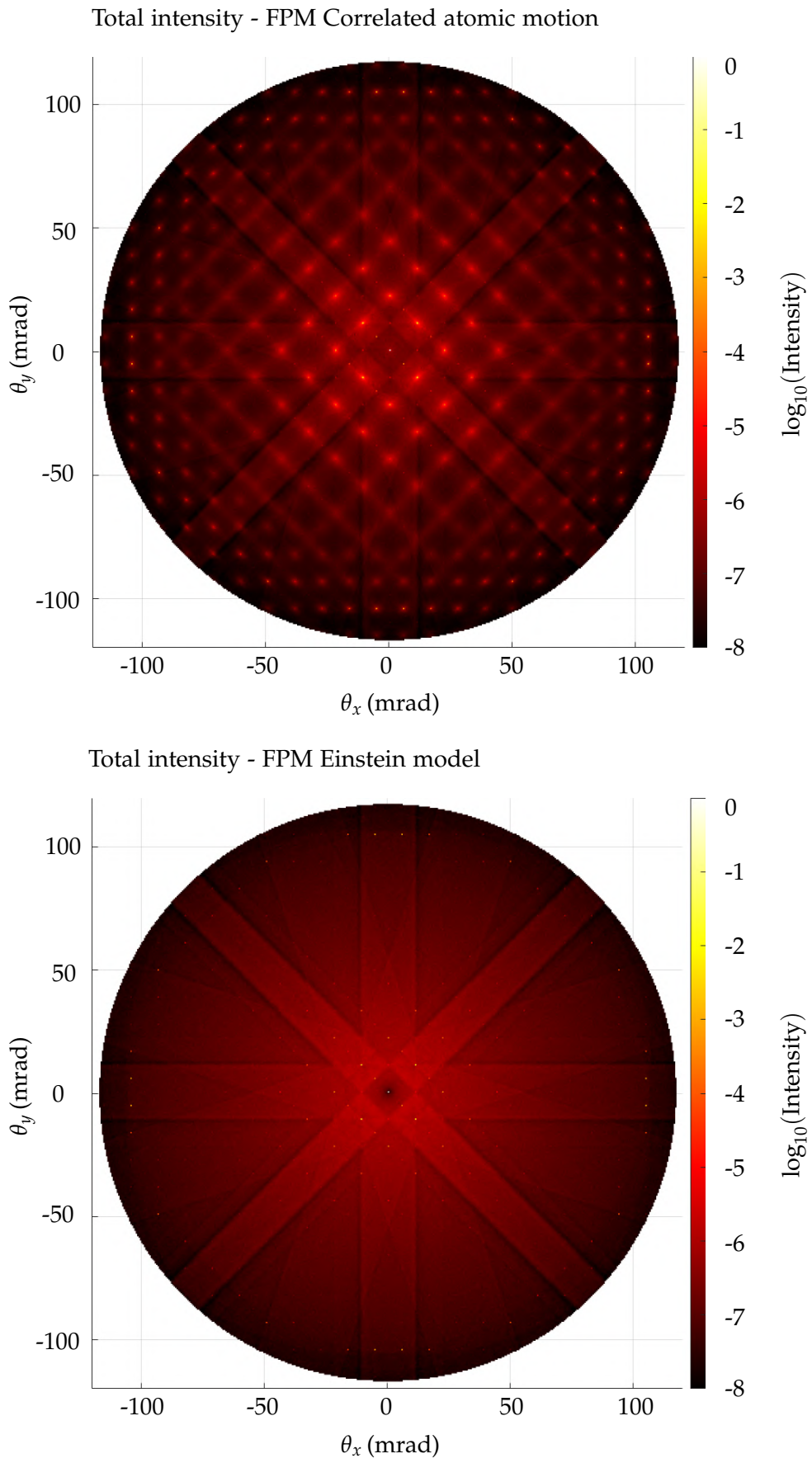

Figure 3.7: Diffraction patterns, total intensity of frozen phonon models for diamond with thickness $t = 50\,\text{nm}$, and electron accelerating voltage $U = 300\,\text{kV}$.

Note that most of the intensity remains in the central Bragg spots, hence, we use the logarithmic scale to highlight the intensity distribution, also the total initial intensity is normalized to be equal to 1. In the complex absorptive potentials model, only Bragg spots are present. However, in the elastic channel of frozen phonon models, we may still notice the background noise, even though the elastic signal should remain in the Bragg spots. This is due to the averaging over the snapshots and the noise is decreasing with increasing number of snapshots. In the TDS signal background visible in total intensity patterns, both frozen phonon models show distinctive Kikuchi lines, which are caused by elastic scattering of inelastically scattered electrons and thus do not fall in the elastic channel. The Kikuchi lines are also more noticeable in the diffraction patterns of thick samples. Furthermore, the Bragg spots vicinity in the correlated atomic motion model exhibits intensity smearing and is brighter than in the Einstein model. Also, higher-order Laue zone Bragg spots are visible around $\theta \approx 100\,\text{mrad}$. The Bragg spot asymmetry in Fig. 3.5 (forbidden reflections) is a very subtle change in Bragg spot intensities caused by the electron beam deformation in transition between the atomic layers in unit cell. It is visible merely because of the broad dynamical range of the plot.

3.3.2 STO Results

Results for STO crystal Figs. 3.8-3.10 continue in the same theme as it was in the case of diamond. We observe sharp Bragg spots in the elastic channels, but we also see some residual TDS background in frozen phonon models. Atoms in STO are, however, much heavier than carbon in a diamond crystal, so in analysis, we will pay great attention to the large scattering angles (Z-contrast HAADF area). Full TDS distribution is then visible in total intensity patterns.

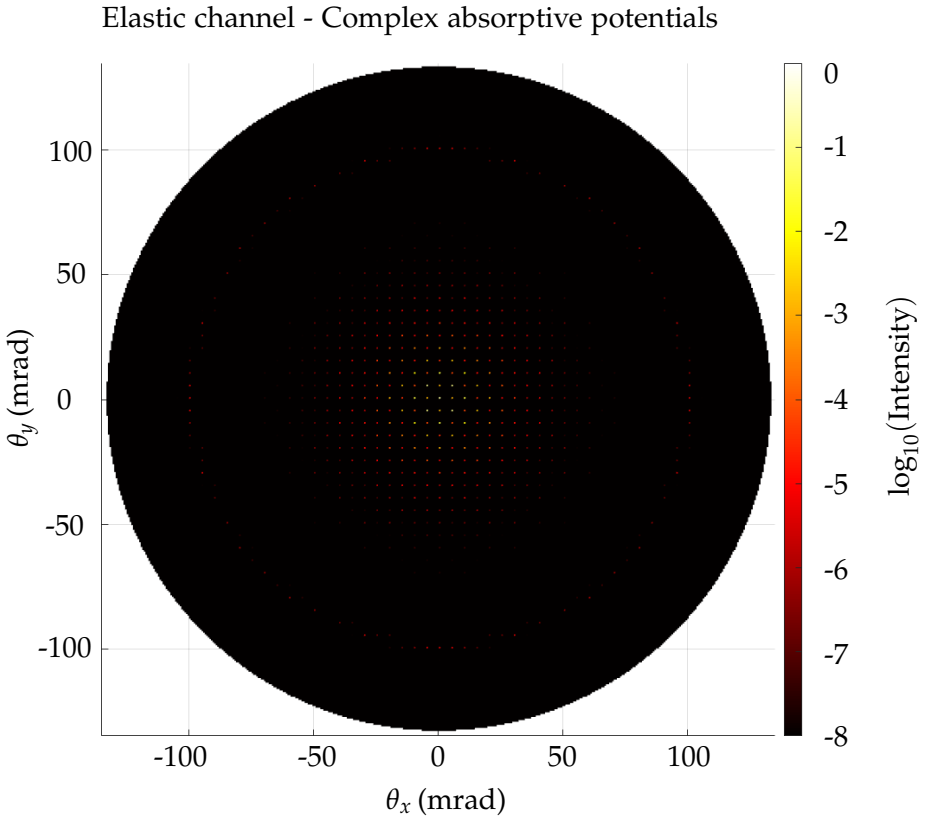

Figure 3.8: Diffraction pattern, elastic channel of complex absorptive potential model for STO with thickness $t = 30\,\text{nm}$, and electron accelerating voltage $U = 300\,\text{kV}$.

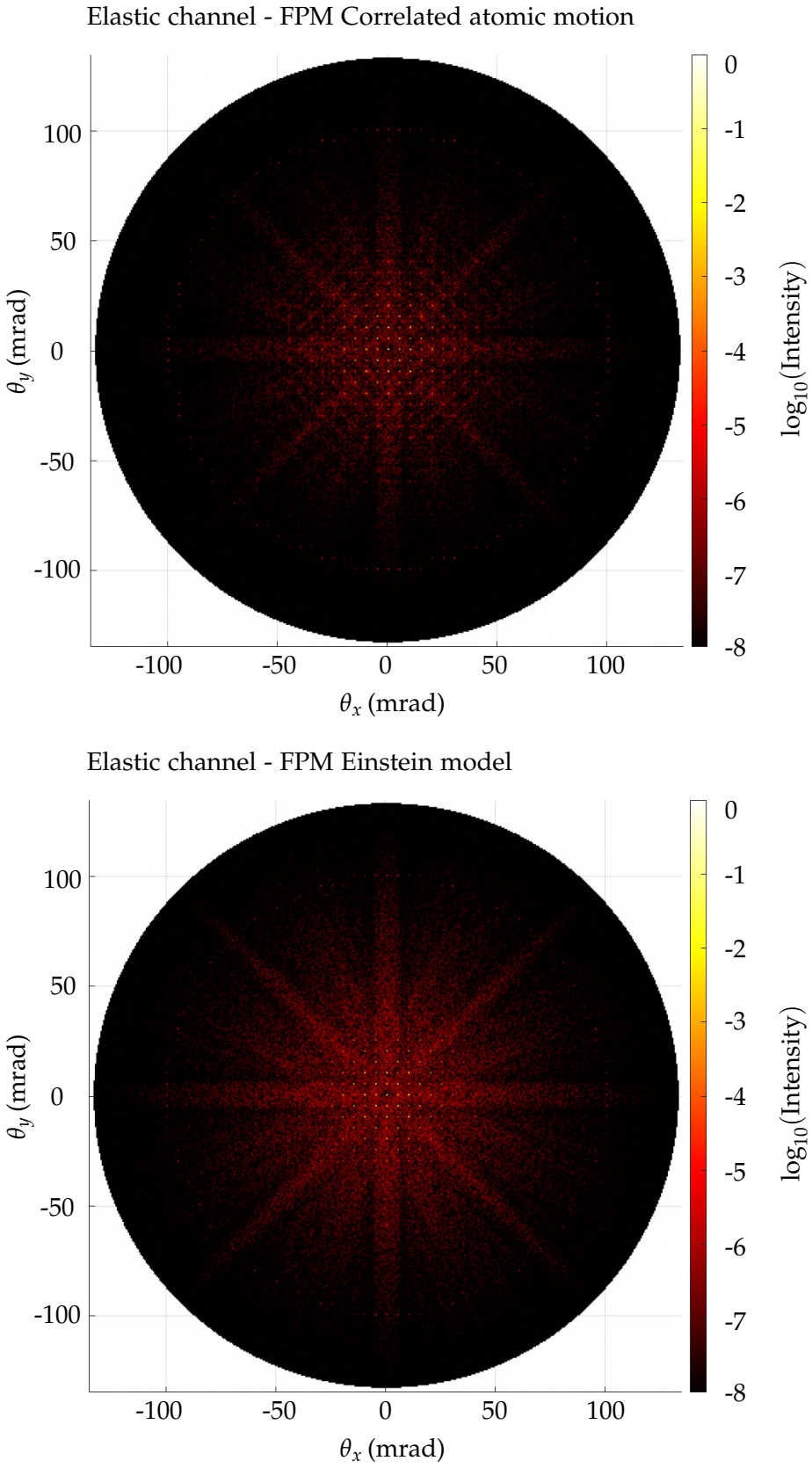

Figure 3.9: Diffraction patterns, elastic channel of frozen phonon models for STO with thickness $t = 30\,\text{nm}$, and electron accelerating voltage $U = 300\,\text{kV}$.

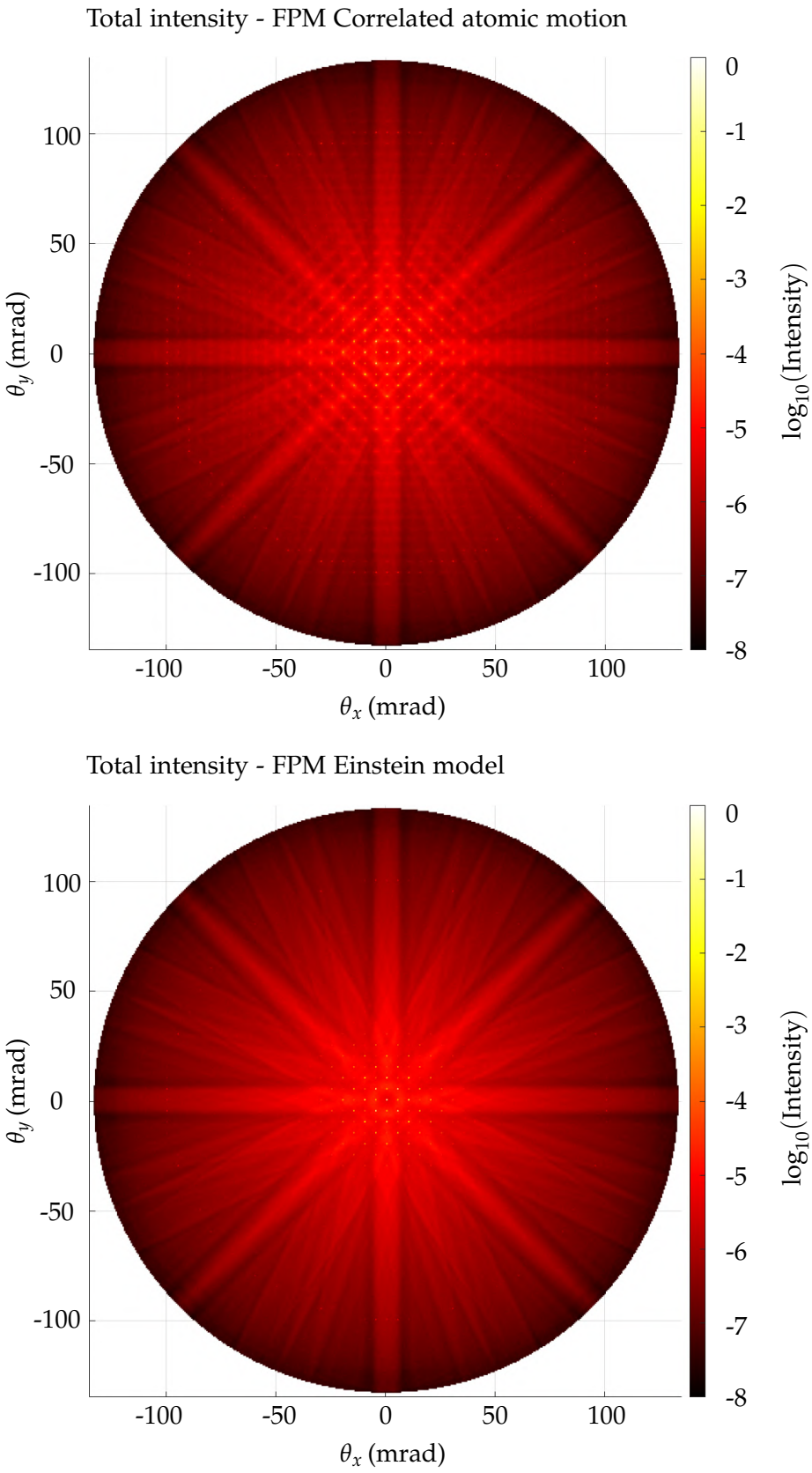

Figure 3.10: Diffraction patterns, total intensity of frozen phonon models for STO with thickness $t = 30\,\text{nm}$, and electron accelerating voltage $U = 300\,\text{kV}$.

3.3.3 Silicon CBED Results of Si (111)

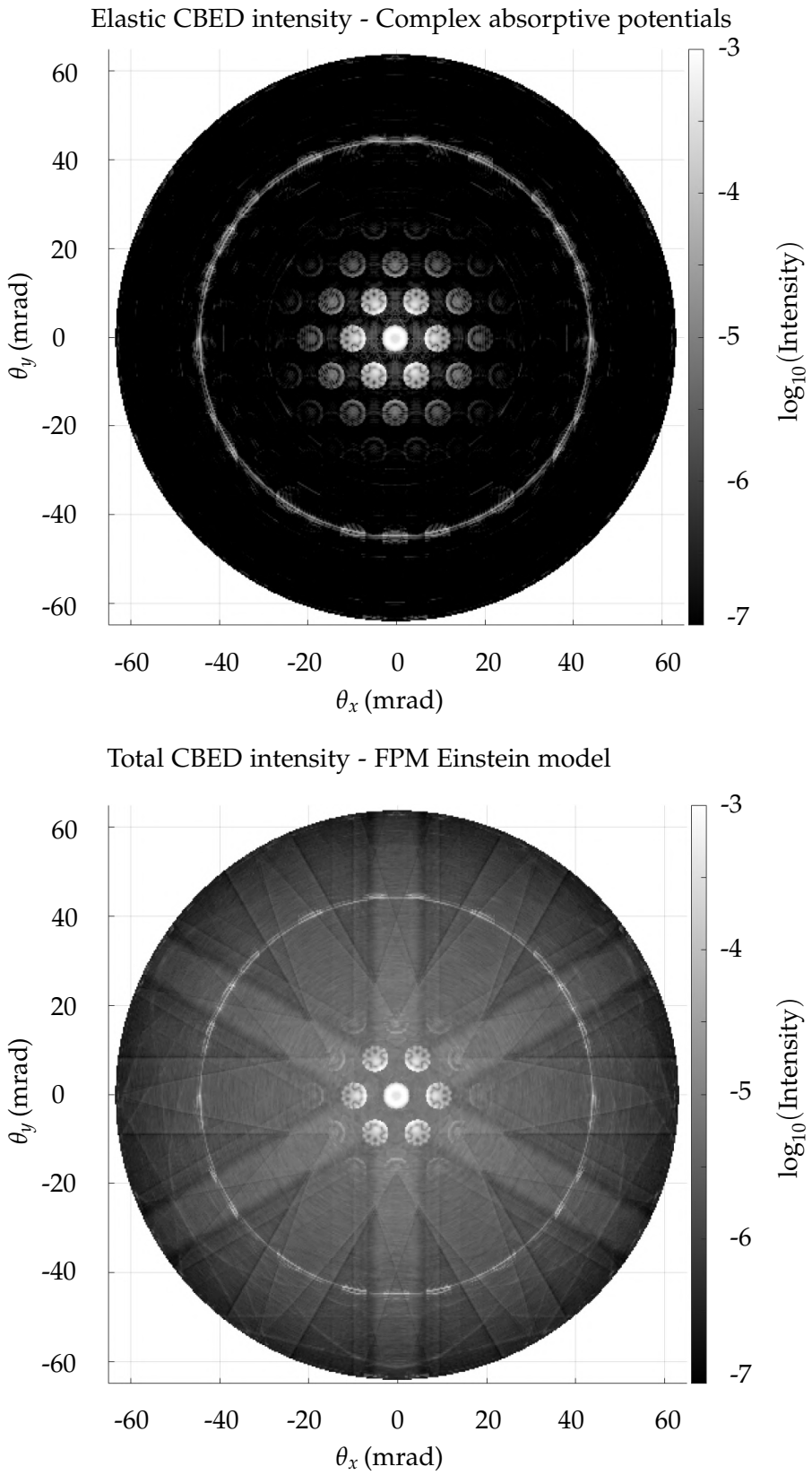

Figure 3.11: Diffraction pattern, elastic channel of complex absorptive model (top) and total intensity of FPM Einstein model (bottom) for Si with thickness $t = 85\,\text{nm}$, electron accelerating voltage $U = 100\,\text{kV}$, and convergence angle 6 mrad.

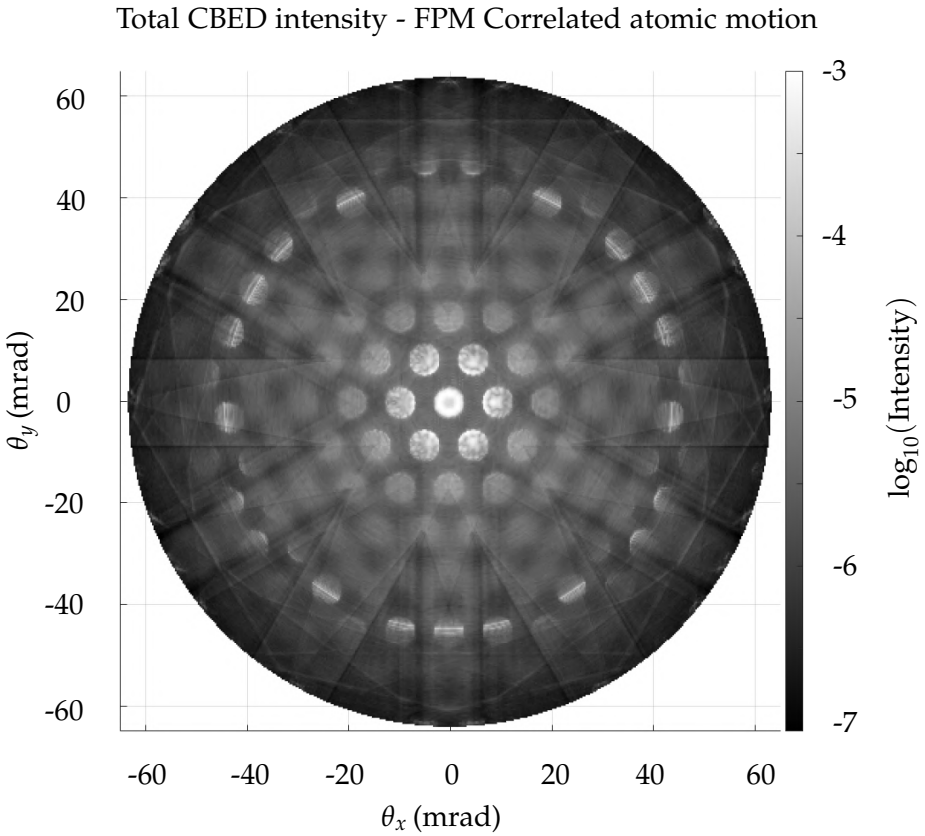

Figure 3.12: Diffraction pattern, total intensity of FPM correlated atomic motion model for Si with thickness $t = 85\,\text{nm}$, electron accelerating voltage $U = 100\,\text{kV}$, and convergence angle 6 mrad.

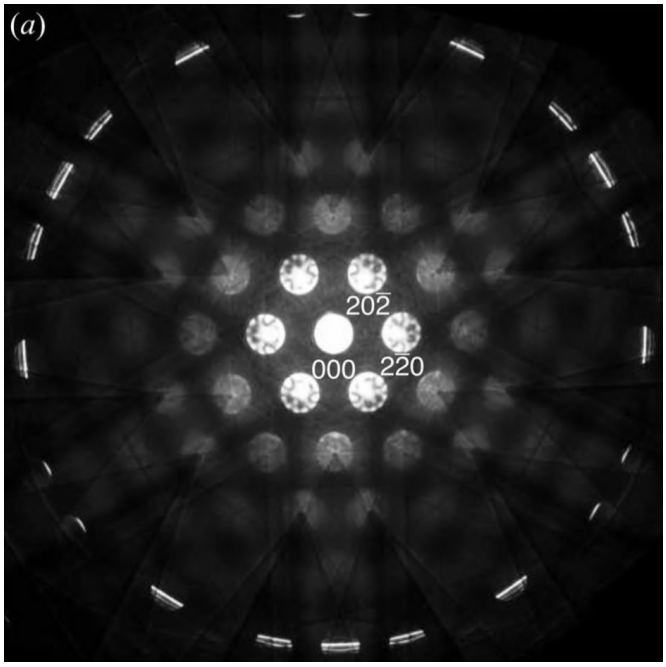

Figure 3.13: Experimental CBED pattern of Si(111) $t \approx 85\,\text{nm}$ as presented by Ogata et al. [52], imaged at 100 kV. The CBED pattern is reprinted from [52] with inverted colormap.

Figs 3.11-3.12 show the CBED simulation results, the dynamical range on the colorscale was slightly adjusted compared to the parallel illumination simulation, since the intensities in Bragg peaks are spread into broader spots. Fig. 3.13 is then reprinted experimental data [52], to compare the diffraction pattern features with the theoretical results. We see that the most of the common features with the experiment has the FPM correlated atomic motion model. It fits in the Bragg disc intensity distribution as well as the TDS shape. The Bragg discs in the Einstein model are swiftly disappearing when going further from the center of the diffraction pattern, and the complex absorption model, in principle, cannot recreate the TDS background.

3.4 Comparison of the Models

We follow up with an analysis of the diffraction pattern results. Since it is impractical to directly subtract and analyze the diffraction models, the methodology of model comparison was carried out as follows: we annularly integrate the diffraction pattern into an intensity profile as depicted in 3.14. The Bragg peaks of the same diffraction angle (which is radius coordinate of the pattern) $\theta = \sqrt{\theta_x^2 + \theta_y^2}$, then project into one peak in the intensity profile; e.g., the value of the four peaks in the same scattering angle is averaged into one. We utilize this fact to compare corresponding peaks among the models. In practice, the discretized dataset of the diffraction pattern is segmented into rings of width exactly one pixel, while we ensure that no pixel is left over, or no pixel is counted multiple times. All pixels in the one ring are then summed up and normalized. The summation of each of the corresponding θ-dependent rings then yields the single value in the intensity profile $I_\mathrm{p}(\theta)$. Doing this for every ring inherently maps the whole intensity profile.

The profiles are shown from all models and all three combinations of model differences $\log_{10}(I_1 - I_2)$, where $1, 2$ represent the arbitrary models. Moreover, for the Diamond and STO crystals, the thickness dependence of the annular profile is presented in 3.4.1.

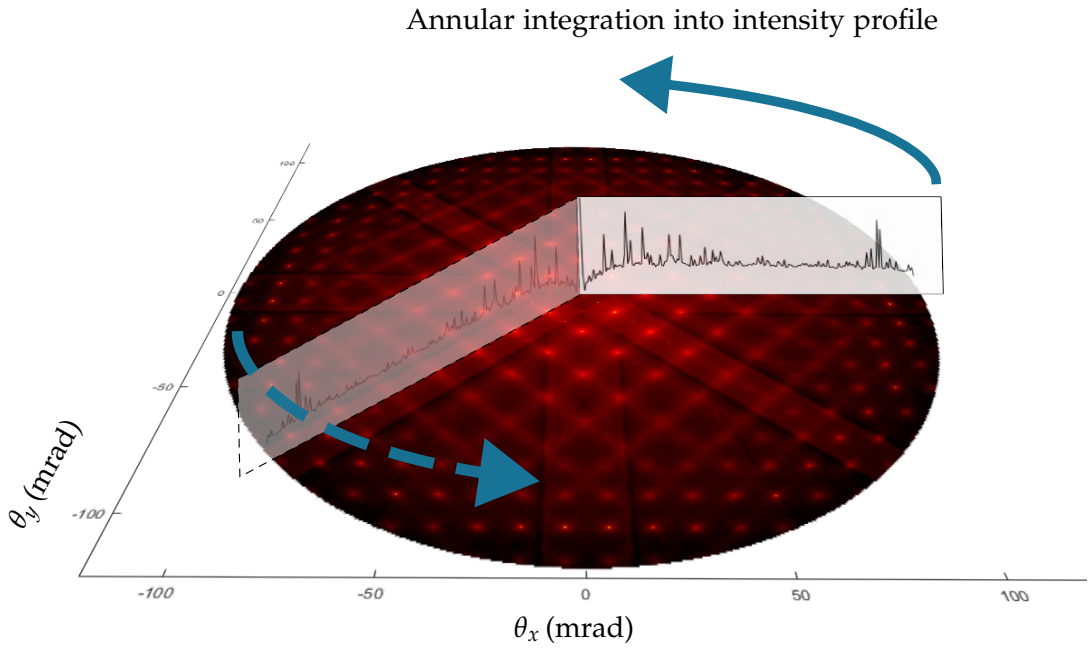

Figure 3.14: Depiction of the annular integration to obtain the intensity profile of the diffraction patterns.

Diamond analysis

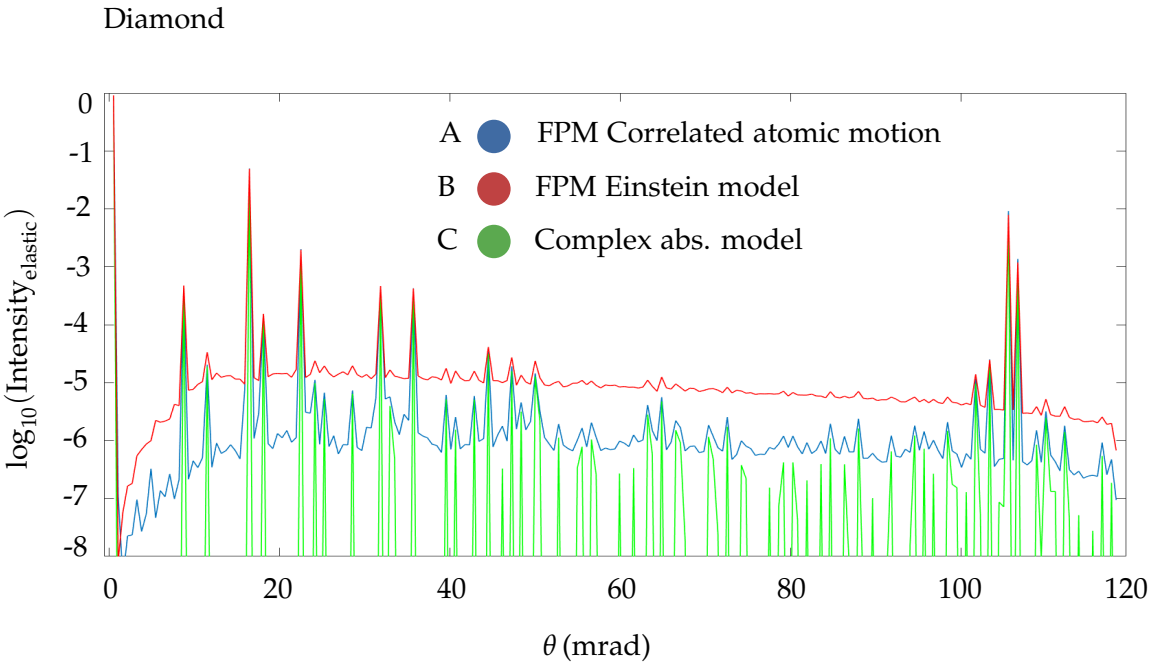

Figure 3.15: Diamond crystal - intensity profiles of the diffraction patterns from all three models.

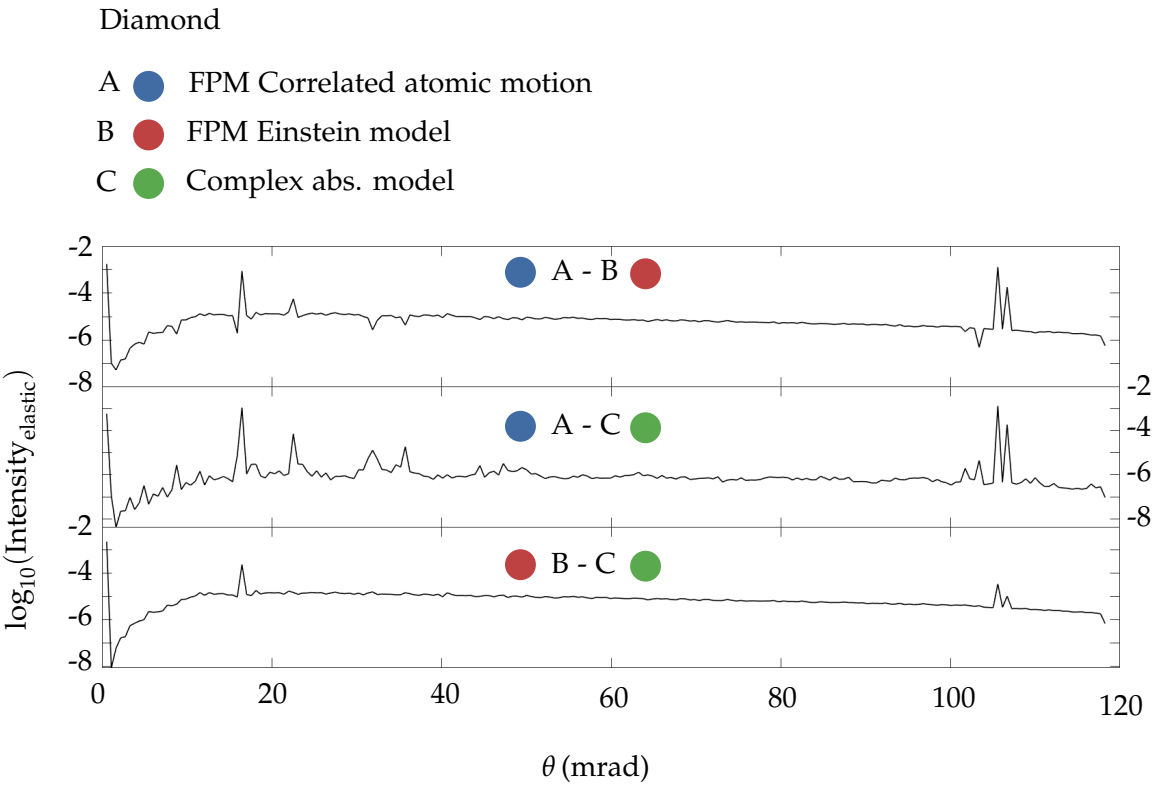

Figure 3.16: Diamond crystal - differences of intensity profiles of the diffraction patterns from all three models.

Fig. 3.15 shows the intensity profiles of diamond to visualize the intensity distribution in the elastic channel. Also note that the scale is again logarithmic. It is apparent that besides the Bragg spots, the TDS background noise still remains present in the frozen phonon models, and has a threshold level in the order of magnitude around $10^{-5}I_0$ in the Einstein model and around $10^{-6}I_0$ in the correlated atomic motion model, where I_0 is the initial intensity. We thus can not compare the models beyond this threshold.

Furthermore, in the case of frozen phonon models, with the addition of more snapshots/variants to the calculations, the Bragg spot intensity value slowly converges. We therefore ensure that the central (and 2nd most intensive) Bragg peak intensity error is well below the observed differences among the models. We observe the evolution of the Bragg spot intensity dependent on the addition of the snapshots. The intensity error is then monitored via the standard deviation value taken from the thermally averaged Bragg peak intensity for the last 50 snapshot additions, and confirmed to be below the typical model difference values in Bragg spots. It has been achieved by providing enough of snapshots to the MSA simulation.

If we compare the differences between the three models in Fig. 3.16, we see that some of the Bragg spots carry an error way above the TDS background noise threshold. We see discrepancies primarily between the FPM correlated atomic motion model and the rest. The Einstein model and complex absorptive model, as presented, should, in theory, be equivalent for an infinite detector area. In certain Bragg spots, including central Bragg spot (0 mrad), this difference is in the order of $10^{-3}I_0$; moreover, after closer inspection, we notice that in the large scattering angles (around 110 mrad) the error is still as significant as in bright field.

There are similar errors near the center of the diffraction pattern as there are in higher-order Laue zone Bragg spots, which are typically weaker in intensity than central Bragg spots. Note the fact that the difference displayed is an absolute error between the models, thus, the relative error in the higher-order Laue zone is significant and may impact HAADF imaging. The error, thus, may be considered as a valid indicator of the discrepancy of the models.

The frozen phonon model is deliberately calculating with atomic motion and shows, that its correspondence to reality is more elaborate [50] than the complex absorptive model. Specific conditions must be met for the models to agree, such as a large collection area, due to the local approximation of the non-local absorptive potential [2]. The large collection area (large detector) can be imitated by convolution of the diffraction pattern with a large kernel matrix Fig. 3.17. For a circular kernel of diameter 110 mrad, the resulting intensity profiles show maximum discrepancies around $10^{-4.5}I_0$, which is an error notably lower than before the convolution. We can thus say that, large collection area increases the precision of the models.

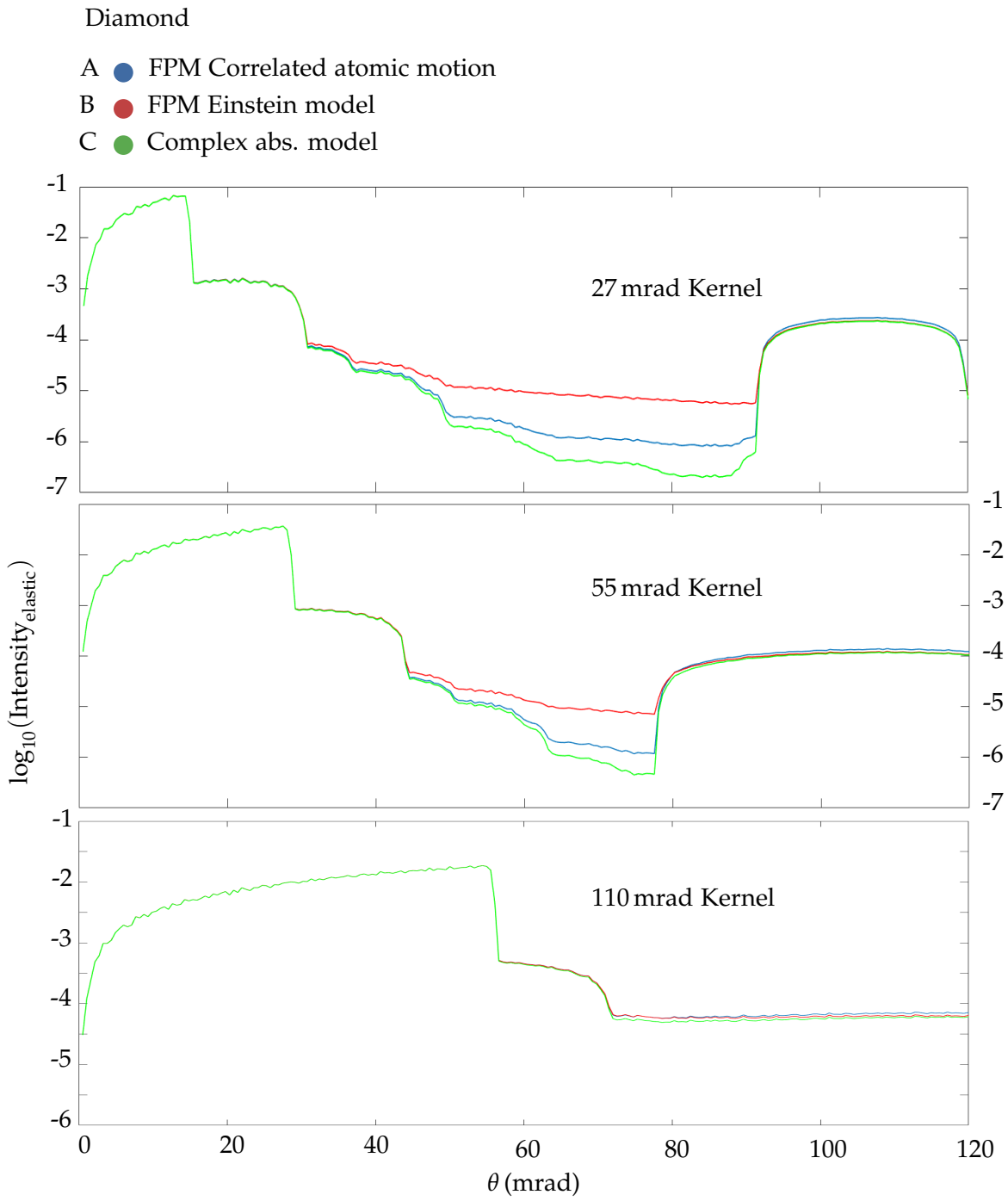

Figure 3.17: Elastic intensity profile for diamond convoluted diffraction patterns, representing a large collection area of 27 mrad, 55 mrad, and 110 mrad in diameter. Note that the intensity profiles for the 110 mrad detector almost overlap.

STO analysis

In STO, the relative difference in signal for the high scattering angle region is also significant, which may result in discrepancies in HAADF simulation. Further, in low angles we see errors in orders of $10^{-1.5} - 10^{-2} I_0$, which are already units of percent. Both of those results are non-negligible. (Fig. 3.19)

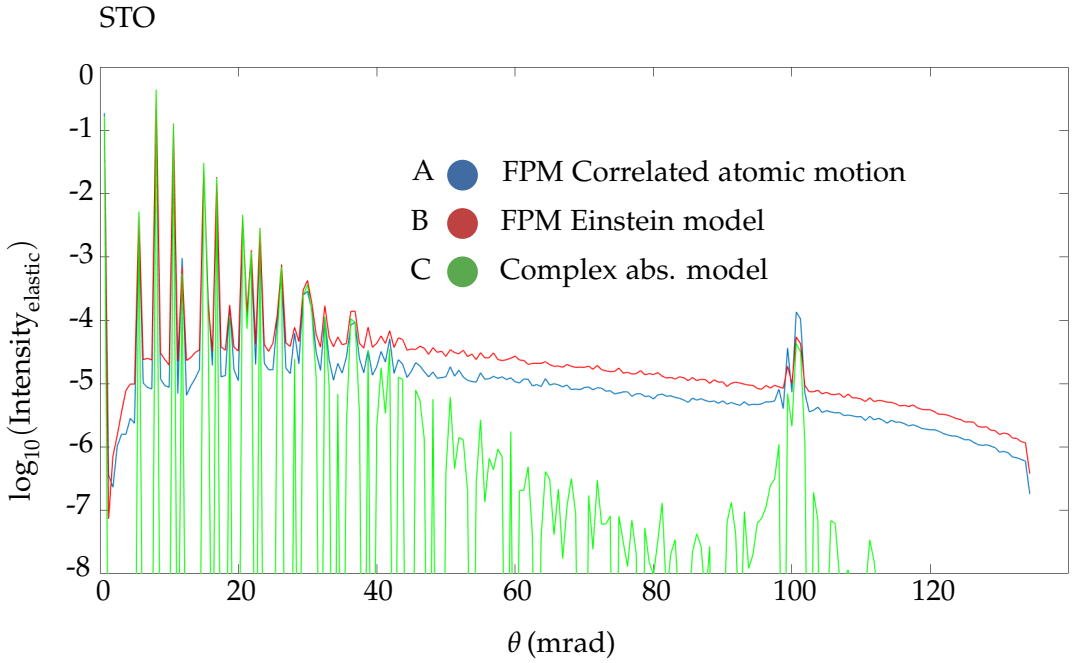

Figure 3.18: STO - intensity profiles of the diffraction patterns from all three models.

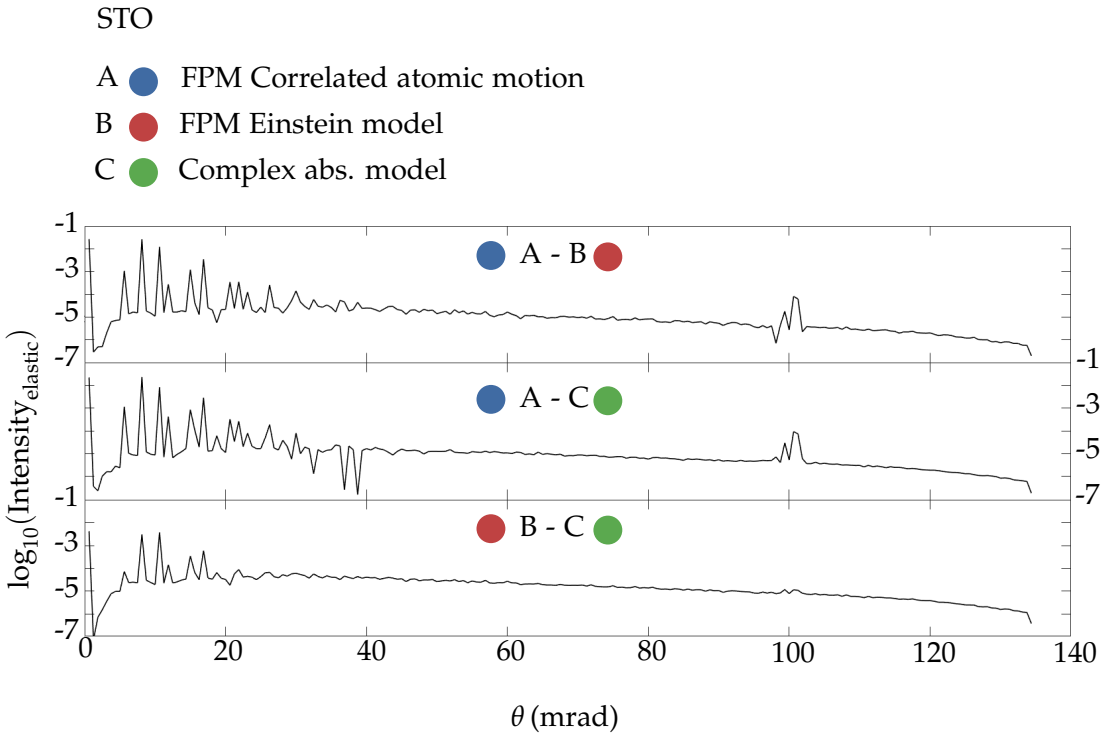

Figure 3.19: STO - differences of intensity profiles of the diffraction patterns from all three models.

Silicon analysis

Primarily due to the broader spot (Bragg discs) in the Silicon STEM CBED simulations, the noise background is higher than in previous cases, this might be resolved by adding more atomic snapshots/variants. However, the peaks in the differences in Fig. 3.21 move in orders $10^{-2} I_0$, which is above the noise, therefore can be considered as a notable error.

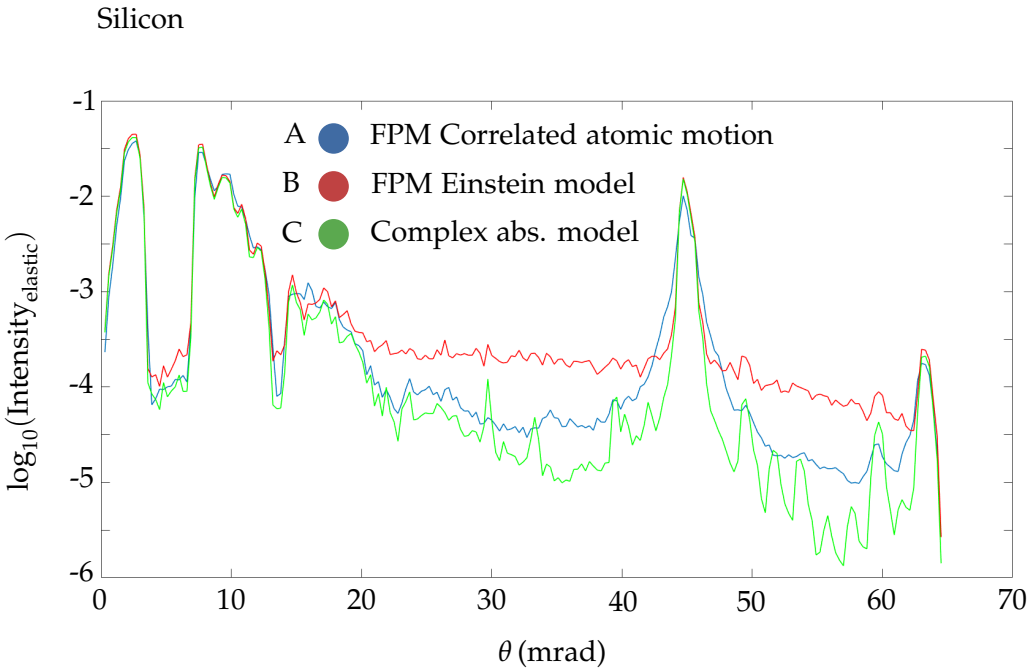

Figure 3.20: Si - elastic intensity profiles of the diffraction patterns from all three models.

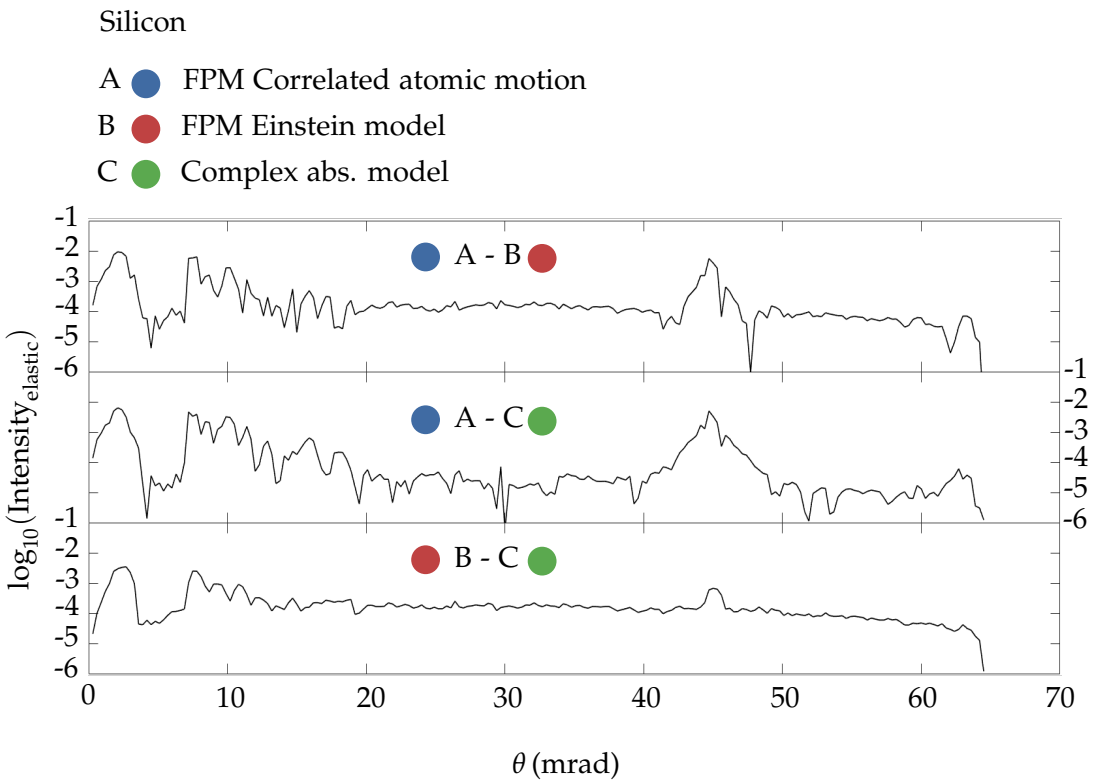

Figure 3.21: Si - differences of elastic intensity profiles of the diffraction patterns from all three models.

3.4.1 Thickness Dependence

The intensity distribution depends heavily on the thickness of the sample. To cover for this dependence, the intensity profiles can be obtained for multiple thickness values and stacked together to create the two-dimensional function Figs. 3.22-3.25. The thickness is sampled into 20 different thickness values. We can see that, in some cases, Bragg spot intensities tend to oscillate with the increasing thickness, and the intensity is, in that case, redistributed into other Bragg spots. The oscillations are directly caused by dynamical diffraction effects. We also see a gradual increase in the TDS background in frozen phonon models, which solely reflects the fact that the inelastic scattering probability grows with sample thickness. In Fig. 3.25 we see increasing errors (between A-B) with thickness at scattering angles around 100 mrad, which indicates a gradual deviation of the models with increasing thickness, it is especially interesting as we only have a 30 nm thick sample.

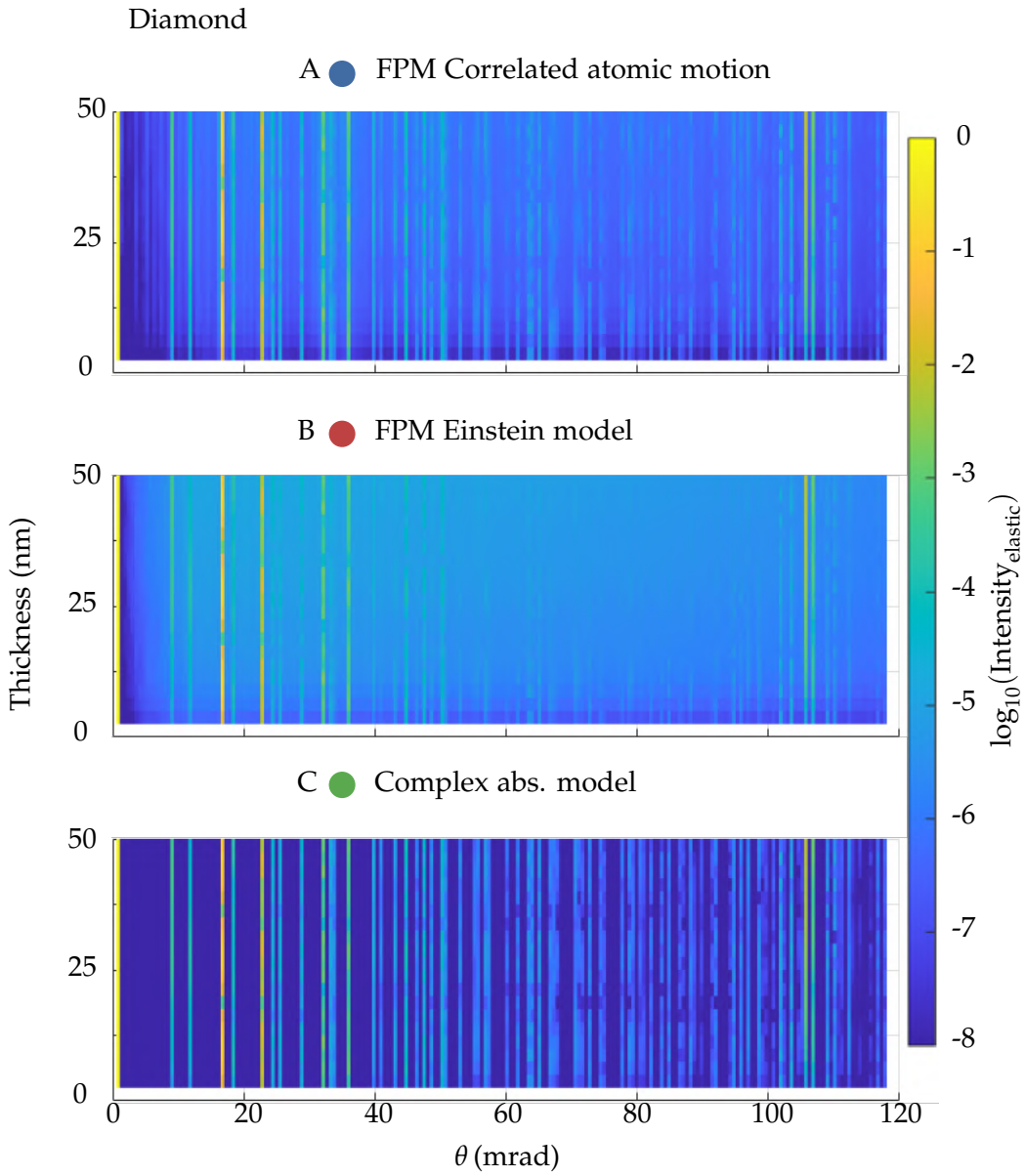

Figure 3.22: Thickness dependence of intensity profiles for diamond crystal.

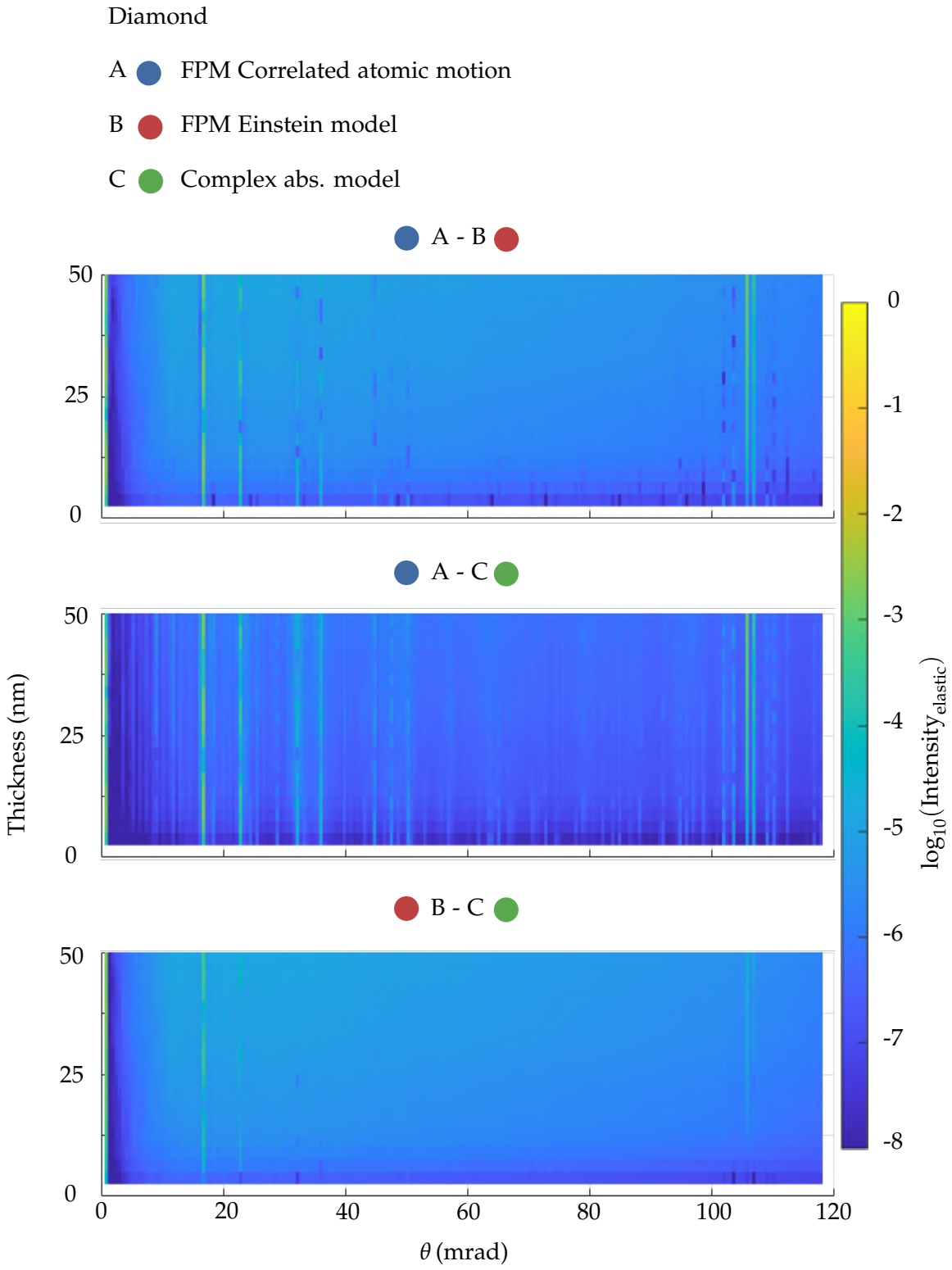

Figure 3.23: Differences among the models, depending on thickness presented in the two-dimensional function for diamond crystal.

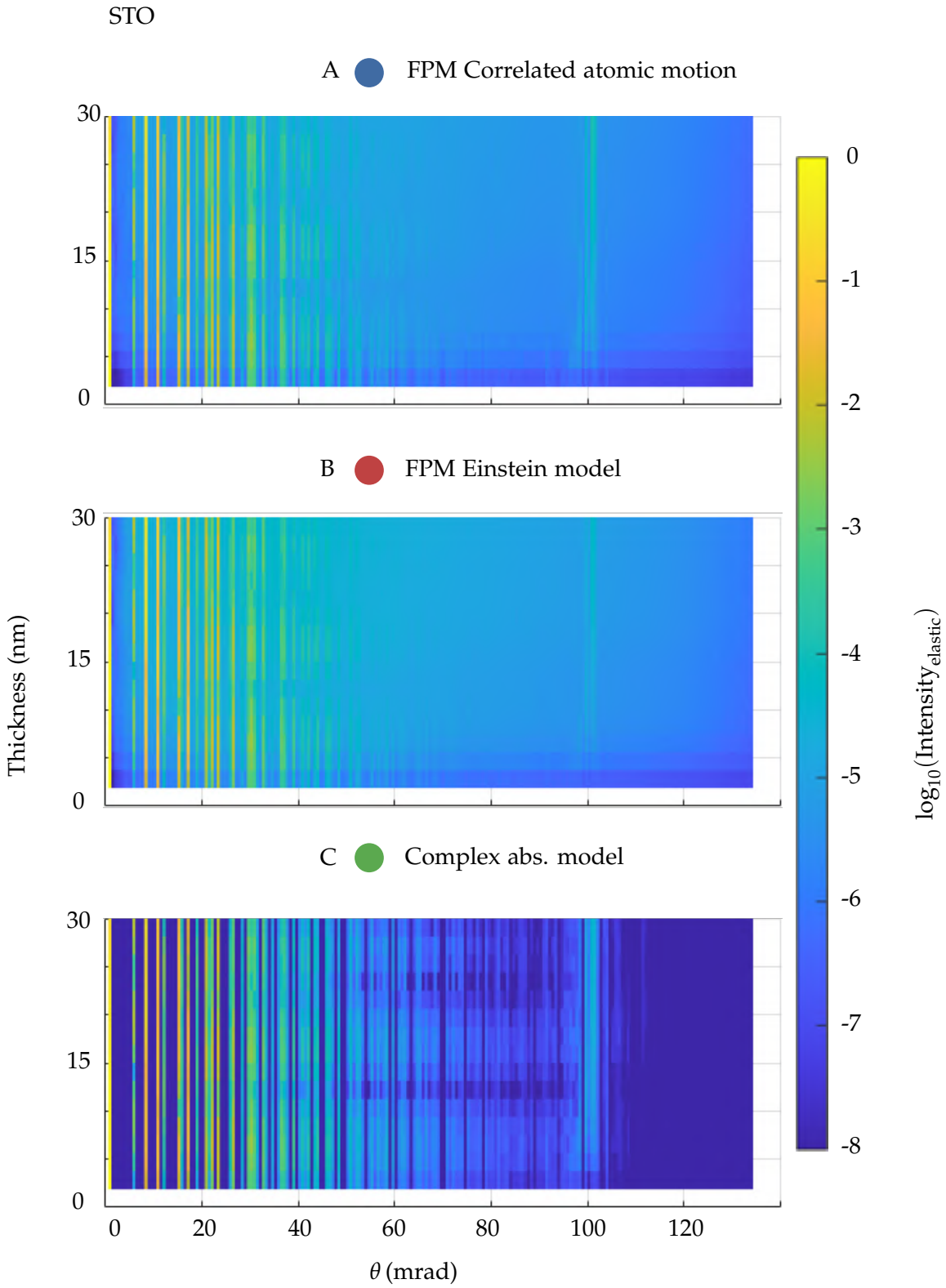

Figure 3.24: Thickness dependence of intensity profiles for STO crystal.

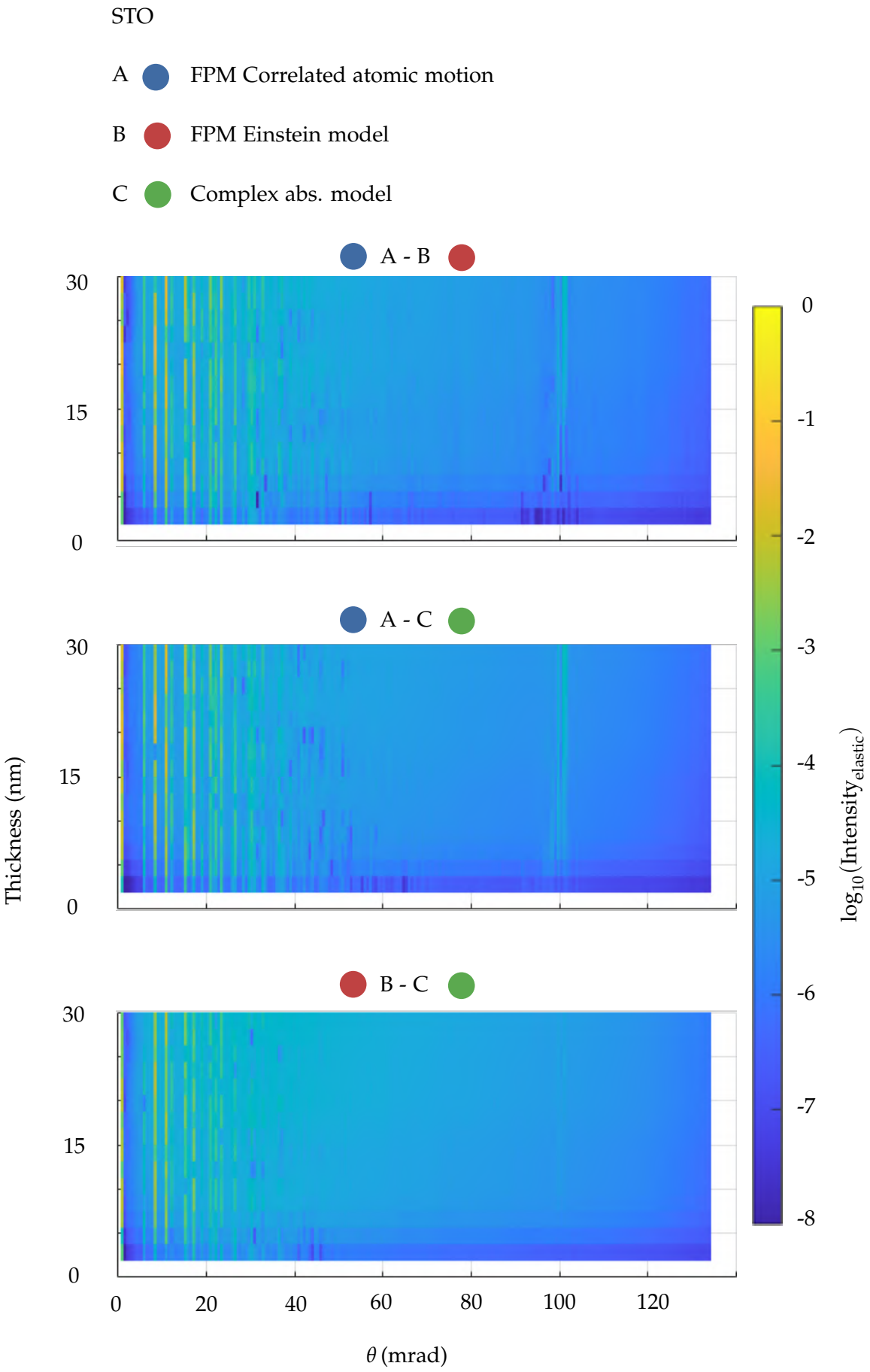

Figure 3.25: Differences among the models, depending on thickness presented in the two-dimensional function for STO crystal.

Summary

The cornerstone of this thesis is to investigate the theory behind the absorptive models of electron scattering in transmission electron microscopy (TEM) and carry out thorough TEM simulations. The approach was divided into multiple systematic stages, to which the thesis chapters of this thesis refer to.

Firstly, the Chapter 1 briefly sums up the fundamental knowledge from transmission electron microscopy and the instrumentation. This helps us to better understand the image formation and types of imaging/diffraction modes, as well as various capabilities or limits of TEM machines. Another very important topic is the electron-specimen interaction, which is a quantum-mechanical phenomenon, and with rigorous mathematical apparatus, we could extract important forms of exciting wavefunctions in the multislice algorithm (MSA).

In Chapter 2, the main focus shifted towards the absorption models on phonon excitations. In total, three absorption models were investigated. Each of the models has a different treatment of the absorptive effects, which are carefully explained. Two of those models come from a so-called frozen phonon model (FPM) theory, and we further divide them into the correlated atomic motion model and the Einstein model. Moreover, for the function of the correlated atomic motion model, it is necessary to implement atomic configurations obtained via molecular dynamics (MD) simulations. The third model is the complex absorptive model described by Yoshioka [13].

The Chapter 3 contains the description of calculation processes and results. Many extensive calculations were carried out. First, it was necessary to define the samples, which were chosen to be diamond crystal, STO crystal, and silicon crystal. The molecular dynamics yielded static lattice configurations, so-called snapshots, which were used in the FPM correlated atomic motion model. The lattice configurations, which come from variants (snapshots) of harmonic atomic motion, were applied in the Einstein model, and lastly complex absorptive model only needs an equilibrium definition of the lattice. As soon as the sample was clearly defined, another set of calculations, this time the MSA, provided us with results in the form of diffraction patterns. Characteristic features of each of the models were then presented on Si crystal convergent beam electron diffraction (CBED) and compared to experimental CBED images, containing typical diffraction features.

All the diffraction patterns were then rigorously analyzed, and many possible variables were taken into account. The intensity profiles of the diffraction patterns were directly compared via subtraction among the three models. In conclusion, the simulation yielded results that show non-negligible differences between the models of frozen

phonon correlated atomic motion model and complex absorptive model, up to units of percent. The errors were investigated to be well above the background noise of frozen phonon models. The FPM Einstein model shows better agreement with the complex absorptive model than the correlated atomic motion model, with absolute errors not exceeding $10^{-2}I_0$. The absolute error was clearly the most significant in the STO crystal, which might indicate the model volatility in terms of atomic masses, as the STO crystal contains heavy elements. Results from light-element diamond crystal calculations also show noticeable errors, however, still not as high as in the case of STO. The relative error is especially significant in the higher-order Laue zone area of the diffraction patterns. We therefore have to be cautious in a simulation of HAADF and HRTEM, while using the complex absorptive model, as the FPM correlated atomic motion is considered more elaborate and closer to real data [50, 16]. The thickness dependence has been presented, and for STO calculations, it shows a gradual increase in errors with greater thickness of the sample.

Even though the discrepancies of the models are in some cases non-negligible, a relatively good agreement of the models has been achieved, provided a large detection area. With the increasing detector area, the errors among the models gradually disappear, as was predicted by [14].

List of Abbreviations

TEM	Transmission electron microscopy (microscope)
STEM	Scanning transmission electron microscopy (microscope)
TDS	Thermal diffuse scattering
HRTEM	High-resolution transmission electron microscopy
ADF	Annular dark-field
HAADF	High-angle annular dark-field
BF	Bright-field
EELS	Electron energy loss spectroscopy
CBED	Convergent beam electron diffraction
HOLZ	Higher-order Laue zone
POA	Phase object approximation
MSA	Multislice algorithm
DWF	Debye-Waller factor
FPM	Frozen phonon model
FPMS	Frozen phonon multislice
MD	Molecular dynamics
DFT	Density functional theory
LAMMPS	Large-scale Atomic/Molecular Massively Parallel Simulator
QEP	Quantum excitation of phonons

Bibliography

1. KRIVANEK, O.L.; DELLBY, N.; LUPINI, A.R. Towards sub-Å electron beams. *Ultramicroscopy*. 1999, vol. 78, no. 1, pp. 1–11. ISSN 0304-3991. Available from DOI: https://doi.org/10.1016/S0304-3991(99)00013-3 (cit. on pp. 1, 3, 8).
2. FINDLAY, Scott D.; OXLEY, Mark P.; ALLEN, Leslie J. Modeling Atomic-Resolution Scanning Transmission Electron Microscopy Images. *Microscopy and Microanalysis*. 2008, vol. 14, no. 1, pp. 48–59. ISSN 1431-9276, ISSN 1435-8115. Available from DOI: 10.1017/S1431927608080112 (cit. on pp. 1, 19, 28, 45).
3. ZEIGER, Paul Michel. *Modeling Vibrational Electron Energy Loss Spectroscopy with the Frequency-Resolved Frozen Phonon Multislice Method*. 2024. ISBN 978-91-513-1987-2. ISSN 1651-6214. PhD thesis. Uppsala University, Materials Theory (cit. on pp. 1, 21).
4. NICHOLLS, R. J.; HAGE, F. S.; MCCULLOCH, D. G.; RAMASSE, Q. M.; REFSON, K.; YATES, J. R. Theory of momentum-resolved phonon spectroscopy in the electron microscope. *Physical Review B*. 2019, vol. 99, no. 9, p. 094105. ISSN 2469-9950, ISSN 2469-9969. Available from DOI: 10.1103/PhysRevB.99.094105 (cit. on p. 1).
5. LUGG, N. R.; FORBES, B. D.; FINDLAY, S. D.; ALLEN, L. J. Atomic resolution imaging using electron energy-loss phonon spectroscopy. *Physical Review B*. 2015, vol. 91, no. 14, p. 144108. ISSN 1098-0121, ISSN 1550-235X. Available from DOI: 10.1103/PhysRevB.91.144108 (cit. on pp. 1, 26).
6. REIMER, Ludwig; KOHL, Helmut. *Transmission electron microscopy: physics of image formation*. 5th ed. New York, NY: Springer, 2008. Springer series in optical sciences, no. 36. ISBN 978-0-387-34758-5 (cit. on pp. 1, 8, 10, 11, 13, 19, 20).
7. KIRKLAND, Earl J. *Advanced Computing in Electron Microscopy*. Boston, MA: Springer US, 2010. ISBN 978-1-4419-6532-5 978-1-4419-6533-2. Available from DOI: 10.1007/978-1-4419-6533-2 (cit. on pp. 1, 14, 15).
8. CHUVILIN, A.; KAISER, U. On the peculiarities of CBED pattern formation revealed by multislice simulation. *Ultramicroscopy*. 2005, vol. 104, no. 1, pp. 73–82. ISSN 03043991. Available from DOI: 10.1016/j.ultramic.2005.03.003 (cit. on p. 1).
9. FORBES, B. D.; ALLEN, L. J. Modeling energy-loss spectra due to phonon excitation. *Physical Review B*. 2016, vol. 94, no. 1, p. 014110. ISSN 2469-9950, ISSN 2469-9969. Available from DOI: 10.1103/PhysRevB.94.014110 (cit. on pp. 1, 26).
10. HALL, C. R.; HIRSCH, P. B. Effect of thermal diffuse scattering on propagation of high energy electrons through crystals. *Proc. R. Soc. Lond.* 1965, vol. 286, pp. 158–177. ISSN 0080-4630. Available from DOI: 10.1098/rspa.1965.0136 (cit. on pp. 1, 19, 26).

11. NIERMANN, Tore. Scattering of fast electrons by lattice vibrations. *Physical Review B*. 2019, vol. 100, no. 14, p. 144305. ISSN 2469-9950, ISSN 2469-9969. Available from DOI: 10.1103/PhysRevB.100.144305 (cit. on p. 2).
12. KRIVANEK, Ondrej L.; LOVEJOY, Tracy C.; DELLBY, Niklas; AOKI, Toshihiro; CARPENTER, R. W.; REZ, Peter; SOIGNARD, Emmanuel; ZHU, Jiangtao; BATSON, Philip E.; LAGOS, Maureen J.; EGERTON, Ray F.; CROZIER, Peter A. Vibrational spectroscopy in the electron microscope. *Nature*. 2014, vol. 514, no. 7521, pp. 209–212. ISSN 0028-0836, ISSN 1476-4687. Available from DOI: 10.1038/nature13870 (cit. on pp. 2, 8).
13. YOSHIOKA, Hide. Effect of Inelastic Waves on Electron Diffraction. *Journal of the Physical Society of Japan*. 1957, vol. 12, no. 6, pp. 618–628. Available from DOI: 10.1143/JPSJ.12.618 (cit. on pp. 2, 19, 24, 26, 27, 53).
14. MARTIN, A. V.; FINDLAY, S. D.; ALLEN, L. J. Model of phonon excitation by fast electrons in a crystal with correlated atomic motion. *Physical Review B*. 2009, vol. 80, no. 2, p. 024308. ISSN 1098-0121, ISSN 1550-235X. Available from DOI: 10.1103/PhysRevB.80.024308 (cit. on pp. 2, 26, 54).
15. ALLEN, L. J.; JOSEFSSON, T. W. Inelastic scattering of fast electrons by crystals. *Physical Review B*. 1995, vol. 52, no. 5, pp. 3184–3198. ISSN 0163-1829, ISSN 1095-3795. Available from DOI: 10.1103/PhysRevB.52.3184 (cit. on pp. 2, 19).
16. VAN DYCK, D. Is the frozen phonon model adequate to describe inelastic phonon scattering? *Ultramicroscopy*. 2009, vol. 109, no. 6, pp. 677–682. ISSN 0304-3991. Available from DOI: https://doi.org/10.1016/j.ultramic.2009.01.001 (cit. on pp. 2, 19, 26, 29, 54).
17. KONG, Ling Ti. Phonon dispersion measured directly from molecular dynamics simulations. *Computer Physics Communications*. 2011, vol. 182, no. 10, pp. 2201–2207. ISSN 00104655. Available from DOI: 10.1016/j.cpc.2011.04.019 (cit. on pp. 2, 22, 29).
18. KNOLL, M.; RUSKA, E. Das Elektronenmikroskop. *Z. Physik*. 1932, vol. 78, pp. 318–339. Available from DOI: 10.1007/BF01342199 (cit. on p. 3).
19. ARDENNE, Manfred von. Das Elektronen-Rastermikroskop. *Z. Physik*. 1938, vol. 109, pp. 553–572. ISSN 0044-3328. Available from DOI: 10.1007/BF01341584 (cit. on p. 3).
20. BROGLIE, Louis de. *Research on the theory of quanta*. Ed. by PETKOV, Vesselin. Montreal, Quebec: Minkowski Institute Press, 2021. ISBN 978-1-927763-98-8 (cit. on p. 3).
21. O'KEEFE, M.A.; HETHERINGTON, C.J.D.; WANG, Y.C.; NELSON, E.C.; TURNER, J.H.; KISIELOWSKI, C.; MALM, J.-O.; MUELLER, R.; RINGNALDA, J.; PAN, M.; THUST, A. Sub-Ångstrom high-resolution transmission electron microscopy at 300keV. *Ultramicroscopy*. 2001, vol. 89, no. 4, pp. 215–241. ISSN 03043991. Available from DOI: 10.1016/S0304-3991(01)00094-8 (cit. on p. 3).
22. BARTHEL, J. Ultra-Precise Measurement of Optical Aberrations for Sub-Ångström Transmission Electron Microscopy, PhD. thesis, Leipzig, 2007 (cit. on p. 5).
23. KRIVANEK, O.L.; AHN, C.C.; WOOD, G.J. The inelastic contribution to high resolution images of defects. *Ultramicroscopy*. 1990, vol. 33, no. 3, pp. 177–185. ISSN 0304-3991. Available from DOI: https://doi.org/10.1016/0304-3991(90)90110-8 (cit. on p. 6).
24. KITTEL, Charles. *Introduction to solid state physics*. 8th ed. Hoboken, NJ: Wiley, 2005. ISBN 978-0-471-41526-8 (cit. on pp. 8, 10, 30, 32).

25. MOTT, Nevill Francis; BRAGG, William Lawrence. The scattering of electrons by atoms. *Proceedings of the Royal Society of London. Series A, Containing Papers of a Mathematical and Physical Character*. 1930, vol. 127, no. 806, pp. 658–665. Available from DOI: 10.1098/rspa.1930.0082 (cit. on p. 10).

26. WIKIPEDIA CONTRIBUTORS. *MottBethe formula — Wikipedia, The Free Encyclopedia*. 2024. Available also from: https://en.wikipedia.org/w/index.php?title=Mott%E2%80%93Bethe_formula&oldid=1240933231 (cit. on p. 10).

27. PENG, L. M.; REN, G.; DUDAREV, S. L.; WHELAN, M. J. Robust Parameterization of Elastic and Absorptive Electron Atomic Scattering Factors. *Acta Crystallographica Section A Foundations of Crystallography*. 1996, vol. 52, no. 2, pp. 257–276. ISSN 01087673. Available from DOI: 10.1107/S0108767395014371 (cit. on pp. 10, 26, 28).

28. SAKURAI, J. J.; NAPOLITANO, Jim. *Modern quantum mechanics*. 2nd ed. Boston: Addison-Wesley, 2011. ISBN 978-0-8053-8291-4 (cit. on pp. 12, 13).

29. DIRAC, P. A. M. *The Principles of Quantum Mechanics*. 3rd. Oxford: Oxford University Press, 1947 (cit. on p. 12).

30. COENE, W.; VAN DYCK, D. The real space method for dynamical electron diffraction calculations in high resolution electron microscopy: III. A computational algorithm for the electron propagation with its practical applications. *Ultramicroscopy*. 1984, vol. 15, no. 4, pp. 287–300. ISSN 0304-3991. Available from DOI: https://doi.org/10.1016/0304-3991(84)90123-2 (cit. on p. 15).

31. BETHE, H. Theorie der Beugung von Elektronen an Kristallen. *Annalen der Physik*. 1928, vol. 392, no. 17, pp. 55–129. Available from DOI: https://doi.org/10.1002/andp.19283921704 (cit. on p. 15).

32. WANG, A.; DE GRAEF, M. Modeling dynamical electron scattering with Bethe potentials and the scattering matrix. *Ultramicroscopy*. 2016, vol. 160, pp. 35–43. ISSN 03043991. Available from DOI: 10.1016/j.ultramic.2015.09.006 (cit. on p. 15).

33. COWLEY, J. M.; MOODIE, A. F. The scattering of electrons by atoms and crystals. I. A new theoretical approach. *Acta Crystallographica*. 1957, vol. 10, no. 10, pp. 609–619. Available from DOI: https://doi.org/10.1107/S0365110X57002194 (cit. on p. 15).

34. BARTHEL, J. Dr. Probe: A software for high-resolution STEM image simulation. *Ultramicroscopy*. 2018, vol. 193, pp. 1–11. ISSN 03043991. Available from DOI: 10.1016/j.ultramic.2018.06.003 (cit. on pp. 15, 28, 33).

35. CAI, Can Ying; ZENG, Song Jun; LIU, Hong Rong; YANG, Qi Bin. Computational comparison of the conventional multislice method and the real space multislice method for simulating exit wavefunctions. *Micron*. 2009, vol. 40, no. 3, pp. 313–319. ISSN 09684328. Available from DOI: 10.1016/j.micron.2008.11.003 (cit. on p. 15).

36. ALLEN, L.J.; DALFONSO, A.J.; FINDLAY, S.D. Modelling the inelastic scattering of fast electrons. *Ultramicroscopy*. 2015, vol. 151, pp. 11–22. ISSN 03043991. Available from DOI: 10.1016/j.ultramic.2014.10.011 (cit. on p. 19).

37. A. MULLER, David; EDWARDS, Byard; J. KIRKLAND, Earl; SILCOX, John. Simulation of thermal diffuse scattering including a detailed phonon dispersion curve. *Ultramicroscopy*. 2001, vol. 86, no. 3-4, pp. 371–380. ISSN 03043991. Available from DOI: 10.1016/S0304-3991(00)00128-5 (cit. on p. 19).

38. CASTELLANOS-REYES, José Ángel; ZEIGER, Paul; BERGMAN, Anders; KEPAPTSOGLOU, Demie; RAMASSE, Quentin M.; IDROBO, Juan Carlos; RUSZ, Ján. Unveiling the impact of temperature on magnon diffuse scattering detection in the transmission electron microscope. *Physical Review B*. 2023, vol. 108, no. 13, p. 134435. ISSN 2469-9950, ISSN 2469-9969. Available from DOI: 10.1103/PhysRevB.108.134435 (cit. on p. 19).

39. ZEIGER, Paul M.; BARTHEL, Juri; ALLEN, Leslie J.; RUSZ, Ján. Lessons from the harmonic oscillator: Reconciliation of the frequency-resolved frozen phonon multislice method with other theoretical approaches. *Physical Review B*. 2023, vol. 108, no. 9, p. 094309. ISSN 2469-9950, ISSN 2469-9969. Available from DOI: 10.1103/PhysRevB.108.094309 (cit. on p. 20).

40. THOMPSON, Aidan P.; AKTULGA, H. Metin; BERGER, Richard; BOLINTINEANU, Dan S.; BROWN, W. Michael; CROZIER, Paul S.; VELD, Pieter J. in 't; KOHLMEYER, Axel; MOORE, Stan G.; NGUYEN, Trung Dac; SHAN, Ray; STEVENS, Mark J.; TRANCHIDA, Julien; TROTT, Christian; PLIMPTON, Steven J. LAMMPS - a flexible simulation tool for particle-based materials modeling at the atomic, meso, and continuum scales. *Computer Physics Communications*. 2022, vol. 271, p. 108171. ISSN 0010-4655. Available from DOI: https://doi.org/10.1016/j.cpc.2021.108171 (cit. on p. 22).

41. EVANS, Denis; HOLIAN, Brad. The NoseHoover thermostat. *The Journal of Chemical Physics*. 1985, vol. 83, pp. 4069–4074. Available from DOI: 10.1063/1.449071 (cit. on p. 22).

42. NGUYEN, Trung Dac. GPU-accelerated Tersoff potentials for massively parallel Molecular Dynamics simulations. *Computer Physics Communications*. 2017, vol. 212, pp. 113–122. ISSN 00104655. Available from DOI: 10.1016/j.cpc.2016.10.020 (cit. on p. 23).

43. HE, Ri; WU, Hongyu; ZHANG, Linfeng; WANG, Xiaoxu; FU, Fangjia; LIU, Shi; ZHONG, Zhicheng. Structural phase transitions in $SrTiO_3$ from deep potential molecular dynamics. *Phys. Rev. B*. 2022, vol. 105, p. 064104. Available from DOI: 10.1103/PhysRevB.105.064104 (cit. on p. 23).

44. RUPP, Matthias. Machine learning for quantum mechanics in a nutshell. *International Journal of Quantum Chemistry*. 2015, vol. 115, no. 16, pp. 1058–1073. ISSN 0020-7608, ISSN 1097-461X. Available from DOI: 10.1002/qua.24954 (cit. on p. 23).

45. CHEN, Xi; KIM, Dennis S.; LEBEAU, James M. A comparison of molecular dynamics potentials used to account for thermal diffuse scattering in multislice simulations. *Ultramicroscopy*. 2023, vol. 244, p. 113644. ISSN 03043991. Available from DOI: 10.1016/j.ultramic.2022.113644 (cit. on p. 23).

46. FORBES, B. D.; MARTIN, A. V.; FINDLAY, S. D.; DALFONSO, A. J.; ALLEN, L. J. Quantum mechanical model for phonon excitation in electron diffraction and imaging using a Born-Oppenheimer approximation. *Physical Review B*. 2010, vol. 82, no. 10, p. 104103. ISSN 1098-0121, ISSN 1550-235X. Available from DOI: 10.1103/PhysRevB.82.104103 (cit. on pp. 24–26).

47. ZEIGER, Paul M.; RUSZ, Ján. Efficient and Versatile Model for Vibrational STEM-EELS. *Physical Review Letters*. 2020, vol. 124, no. 2, p. 025501. ISSN 0031-9007, ISSN 1079-7114. Available from DOI: 10.1103/PhysRevLett.124.025501 (cit. on pp. 24, 25).

48. WEICKENMEIER, A.; KOHL, H. Computation of absorptive form factors for high-energy electron diffraction. *Acta Crystallographica Section A Foundations of Crystallography*. 1991, vol. 47, no. 5, pp. 590–597. ISSN 01087673. Available from DOI: 10.1107/S0108767391004804 (cit. on pp. 26, 28, 33).

49. VAN DEN BROEK, W.; JIANG, X.; KOCH, C.T. FDES, a GPU-based multislice algorithm with increased efficiency of the computation of the projected potential. *Ultramicroscopy*. 2015, vol. 158, pp. 89–97. ISSN 03043991. Available from DOI: 10.1016/j.ultramic.2015.07.005 (cit. on p. 29).

50. BISKUPEK, J; CHUVILIN, A; KAISER, U. Evaluation of Frozen Phonons Models for Multislice Calculation of TDS. *Microscopy and Microanalysis* [online]. 2007, vol. 13, no. S03, pp. 130–131 [visited on 2024-07-15]. ISSN 1431-9276, ISSN 1435-8115. Available from DOI: 10.1017/S1431927607080658 (cit. on pp. 29, 45, 54).

51. WIKIPEDIA CONTRIBUTORS. *Lattice constant — Wikipedia, The Free Encyclopedia*. 2025. Available also from: https://en.wikipedia.org/w/index.php?title=Lattice_constant&oldid=1279184374 (cit. on p. 31).

52. OGATA, Yoichiro; TSUDA, Kenji; TANAKA, Michiyoshi. Determination of the electrostatic potential and electron density of silicon using convergent-beam electron diffraction. *Acta Crystallographica Section A*. 2008, vol. 64, no. 5, pp. 587–597. Available from DOI: https://doi.org/10.1107/S0108767308021338 (cit. on pp. 42, 43).